

Sprites produced by quasi-electrostatic heating and ionization in the lower ionosphere

V. P. Pasko, U. S. Inan, and T. F. Bell

STAR Laboratory, Stanford University, Stanford, California

Y. N. Taranenko

XCM, Computational Science Methods, Los Alamos National Laboratory, Los Alamos, New Mexico

Abstract. Quasi-electrostatic (QE) fields that temporarily exist at high altitudes following the sudden removal (e.g., by a lightning discharge) of thundercloud charge at low altitudes lead to ambient electron heating (up to ~ 5 eV average energy), ionization of neutrals, and excitation of optical emissions in the mesosphere/lower ionosphere. Model calculations predict the possibility of significant (several orders of magnitude) modification of the lower ionospheric conductivity in the form of depletions of electron density due to dissociative attachment to O_2 molecules and/or in the form of enhancements of electron density due to breakdown ionization. Results indicate that the optical emission intensities of the 1st positive band of N_2 corresponding to fast (~ 1 ms) removal of 100–300 C of thundercloud charge from 10 km altitude are in good agreement with observations of the upper part (“head” and “hair” [Sentman *et al.*, 1995]) of the sprites. The typical region of brightest optical emission has horizontal and vertical dimensions ~ 10 km, centered at altitudes 70 km and is interpreted as the head of the sprite. The model also shows the formation of low intensity glow (“hair”) above this region due to the excitation of optical emissions at altitudes ~ 85 km during $\sim 500 \mu s$ at the initial stage of the lightning discharge. Comparison of the optical emission intensities of the 1st and 2nd positive bands of N_2 , Meinel and 1st negative bands of N_2^+ , and 1st negative band of O_2^+ demonstrates that the 1st positive band of N_2 is the dominating optical emission in the altitude range around ~ 70 km, which accounts for the observed red color of sprites, in excellent agreement with recent spectroscopic observations of sprites. Results indicate that the optical emission levels are predominantly defined by the lightning discharge duration and the conductivity properties of the atmosphere/lower ionosphere (i.e., relaxation time of electric field in the conducting medium). The model demonstrates that for low ambient conductivities the lightning discharge duration can be significantly extended with no loss in production of optical emissions. The peak intensity of optical emissions is determined primarily by the value of the removed thundercloud charge and its altitude. The preexisting inhomogeneities in the mesospheric conductivity and the neutral density may contribute to the formation of a vertically striated fine structure of sprites and explain why sprites often repeatedly occur in the same place in the sky as well as their clustering. Comparison of the model results for different types of lightning discharges indicates that positive cloud to ground discharges lead to the largest electric fields and optical emissions at ionospheric altitudes since they are associated with the removal of larger amounts of charge from higher altitudes.

1. Introduction

Sprites are luminous glows occurring above thunderstorms at altitudes typically ranging from ~ 50 to 90 km.

In video, they exhibit a red color at their top which gradually changes to blue at lower altitudes. Sprites may occur singly or in clusters of two or more [Sentman *et al.*, 1995]. The lateral extent of “unit” sprites is typically 5–10 km, and they endure for several milliseconds. Another form of recently discovered optical flashes above thunderstorms are blue jets, or jets in short, which are upward moving (~ 100 km/s) highly

Copyright 1997 by the American Geophysical Union.

Paper number 96JA03528.
0148-0227/97/96JA-03528\$09.00

collimated beams of luminosity, emanating from the tops of thunderclouds, extending up to ~ 50 km altitude and exhibiting a primarily blue color [Wescott *et al.*, 1995a]. In this paper we concentrate on investigation of sprite phenomena.

Below we briefly survey the information available concerning the recently discovered phenomena of sprites. The intent of the survey is to give the reader a general understanding of the observed properties of the phenomenon of sprites which constitute an important component of the complex of physical processes which are not yet fully understood and which manifest upward electrodynamic coupling of energy originating in tropospheric thunderstorms to the mesosphere and lower ionosphere.

1.1. Experimental Evidence of Upward Coupling of Thunderstorms

During the past several years, a wealth of new experimental evidence has surfaced which indicates strong electrodynamic coupling between phenomena occurring in the troposphere at altitudes of 10–15 km and the mesosphere/lower ionosphere ranging in altitude up to 100 km. This experimental evidence includes early/fast perturbations of subionospherically propagating VLF signals associated with lightning discharges in underlying thunderstorms [Armstrong, 1983; Inan *et al.*, 1988, 1993, 1995, 1996a; Dowden *et al.*, 1994] and optical emissions in clear air above thunderstorms associated with sprites [e.g., Sentman *et al.*, 1995; Lyons, 1994, 1995, 1996; Boeck *et al.*, 1995; Rairden and Mende, 1995; Winckler *et al.*, 1996], blue jets [Wescott *et al.*, 1995a], blue starters [Wescott *et al.*, 1995b, 1996], and airglow enhancements [Boeck *et al.*, 1992]. The latter are believed to be closely associated with recently discovered rapid (< 1 ms) optical emissions at 80–95 km altitudes with lateral extents up to 300 km preceding sprites and referred to as “elves” [Fukunishi *et al.*, 1996; Lyons, 1996; Inan *et al.*, 1996b]. The first observations of gamma ray bursts of terrestrial origin [Fishman *et al.*, 1994], associated with positive cloud-to-ground lightning discharges [Inan *et al.*, 1996c], and intense wide-band VHF bursts [e.g., Holden *et al.*, 1995] constitute additional new examples of upward coupling of energy originating in thunderstorms.

1.2. First Recorded Observations of Optical Flashes Above Thunderstorms

The first recorded image of unusual optical flashes occupying large volumes of space above thunderstorms was obtained serendipitously on July 5, 1989, during a test of a low-light-level TV camera at the O'Brien Observatory of the University of Minnesota near Minneapolis by Franz *et al.* [1990]. The image, which persisted less than one video frame (< 30 ms), resembled two plume discharges simultaneously extending into the clear sky above a thunderstorm [Franz *et al.*, 1990].

Following the original observation by Franz *et al.* [1990], Vaughan *et al.* [1992], and Boeck *et al.* [1995]

reported video observations from the space shuttle of tens of similar optical events. Most of the video examples captured from space have the appearance of thin luminous filaments of glowing gases stretching into the stratosphere above thunderstorm [Boeck *et al.*, 1995]. Typical heights of optical flashes were estimated to be 60 to 75 km above the Earth with the uncertainty arising from the rather coarse resolution of the digitized image and from the lack of information on the cloud top height or the location at which the stratospheric flash intersects the cloud top [Boeck *et al.*, 1995]. The lateral width of observed luminosities varied considerably between events, with some examples showing thin or several thin vertical filaments while others appearing as broad columns of some kilometers across. In addition, many events exhibited a bulge of luminosity at the top of the flash with dimensions of order of kilometers [Boeck *et al.*, 1995]. The full vertical extent of the flashes was only observable within the time resolution of one video field (17 ms) [Boeck *et al.*, 1995]. It appears from the space shuttle observations that the conditions for the stratospheric flashes may occur over most regions of the globe (in temperate and tropical areas, over the oceans, and over the land) and that the luminosity is definitely associated with a discharge in the cloud below and occurs soon after the onset of the discharge [Boeck *et al.*, 1995].

1.3. Observations During Summer 1993

Using a low-light level all sky black and white television system, Sentman and Wescott [1993] imaged 19 examples of optical flashes during a single flight of NASA's DC-8 airborne laboratory over thunderstorms in Iowa, Nebraska, and Kansas in July 1993. They estimated the terminal heights of the events to be 60 km, with error bars (due to unknown range) extending to 100 km. The duration of the flashes was estimated to be 16 ms or less, and the brightness as calculated from comparison with stellar brightness to be 25–50 kR, roughly that of moderately bright aurorae. The emission volume of flashes was estimated to be > 1000 km³, with a horizontal extent of ~ 10 –50 km and their occurrence rate was such that an optical flash was observed in association with every 200–300th cloud-to-ground stroke.

In a ground-based program in the high plains area of Fort Collins, Colorado, Lyons [1994] obtained black and white images of high altitude flashes above storm systems in Nebraska and Kansas in July and August 1993. An image-intensified, low-light video camera systematically monitored the stratosphere above distant (100–800 km range) mesoscale convective systems over the high plains of the central United States for 21 nights between July 6 and August 27, 1993. Complex, luminous structures were observed above large thunderstorm clusters on eleven nights, with one storm system (July 7, 1993) yielding 248 events in 410 min. The duration of events ranged from 33 to 283 ms, with an average of 98 ms. The luminous structures, generally not visible to the naked, dark-adapted eye, exhibited on video a wide variety of brightness levels and shapes including

streaks, aurora-like curtains, smudges, fountains, and jets. The structures were often more than 10 km wide and their upper portions extended to above 50 km altitude. Some of the shapes appeared to be "frozen in space" as if "illuminated" during the few video fields in which they were visible. The video images, with a time resolution of 17 ms per video field, did not provide any sense of propagation either upward or downward. With heights reaching towards 100 km and diameters of 20 km or more, assuming circular symmetry, it appears that the larger luminous structures can attain emission volumes of thousands of cubic kilometers. While the mesoscale convective system as a whole is electrically active, mesospheric optical flashes tend to occur in regions characterized by low cloud-to-ground flash rates where positive cloud-to-ground flashes are more common [Lyons, 1994].

Winckler [1995] observed more than 150 optical flashes above a thunderstorm complex moving south-east across the state of Iowa during the night of August 9-10, 1993. Black and white images were obtained through clear air with an intensified CCD TV cameras at the O'Brien Observatory of the University of Minnesota located about 60 km north east of Minneapolis and 250-500 km from the storm center. The optical flashes consisted of bright vertical striations extending from 50 to 80 km altitude, often covering tens of kilometers laterally, with tendrils of decreasing intensity visible in the brighter events down to the cloud tops below 20 km altitude. All of the more intense events were coincident with a VLF sferic (i.e., powerful impulsive radio signal radiated by intense return stroke currents involved in a lightning discharge) measured in the 300 Hz to 12 kHz range, but smaller events often did not occur in association with a detectable sferic. The intense part of the events usually occurred within one TV field (16.7 ms). The brightness for the more intense events was estimated to be 50-100 kR. Comparison of results obtained with those reported by Vaughan *et al.* [1992], Sentman and Wescott [1993], and Lyons [1994] led Winckler [1995] to conclude that all these authors were indeed observing the same phenomena.

1.4. Terminology of Optical Flashes Above Thunderstorms

The optical flashes above thunderstorms have from the beginning been variously referred to in the literature as "upward," "cloud-to-stratosphere," or "cloud-to-ionosphere" lightning discharges. Use of these terms invokes of unwarranted parallels to normal tropospheric lightning, and also implies an upward direction of propagation which has not yet been determined (see discussion by Lyons [1994] and Sentman *et al.* [1995]). The term "sprite" has been suggested by D. Sentman [e.g., Sentman *et al.*, 1995] as nonjudgmental as to the physics of the phenomenon and the specific production mechanisms. All of the above described optical flashes, including those observed from the space shuttle, might qualify for inclusion in the broad category of sprites.

1.5. Observations During Summer 1994

The first color imagery of optical flashes above thunderstorms and their unambiguously triangulated physical dimensions and heights were obtained using observations from two jet aircraft [Sentman *et al.*, 1995; Wescott *et al.*, 1995a; Sentman and Wescott, 1994, 1995]. Low-light level television images, in both color and black and white, show that there are at least two distinctly different types of optical emissions spanning part or all of the distance between the anvil tops of the thunderclouds and the ionosphere. The first of these emissions, called sprites, are luminous structures of brief (typically < 16 ms although some events endure longer) duration with a main body in red color that typically span the altitude range of 50-90 km, and lateral dimensions of 5-30 km. Faint bluish tendrils often extended downward from the main body of sprites, occasionally appearing to reach the cloud tops near 20 km. The brightest red region of a unit sprite, its "head," lies between the characteristic altitudes of 66 and 74 km. Above the head there is often a dark band ("hairline") above which a faint, wispy red glow ("hair") is observed to splay upward and outward toward terminal altitude. Beneath the head there sometimes occurs a dark band ("collar") at 66 ± 4 km below which faint tendrils may extend downward to altitudes of 40-50 km, changing from red near the collar to blue at their lowest extremities. Sprites may occur singly but more typically occur in clusters of two or more. Clusters may be tightly packed together into large structures 40 km or more across, or loosely spread out into distended structures of spatially separated sprites. The onset of luminescence occurs simultaneously (within video resolution of ~ 16 ms) across the cluster as a whole, coincident with the occurrence of cloud-to-ground lightning below. All elements of the cluster typically decay in unison in 100-160 ms, but most of this decay time may be attributed to the image lag of the video cameras [Sentman *et al.*, 1995]. Sprites seem preferentially to occur on the backside of frontal storm systems and occur in regions of positive lightning ground strokes.

Observations of sprites from the Yucca Ridge Field Station 29 km northeast of Fort Collins, Colorado, on the night of July 11-12, 1994, were performed by Winckler *et al.* [1996] using both wide-field and telescopic image-intensified CCD TV cameras, a telescopic photometer system and a 1 to 50 kHz broad band VLF sferic receiver. Telescopic TV images of bright sprites had a fan shaped upper plume with not well resolved fine features, as well as upward forked and vertically striated forms adjacent to these plumes and bright points of luminosity around the plume shaped regions. Many sprites consisted entirely of groups of vertically aligned striations which sometimes appeared to diverge from a common point of origin at cloud tops. All observed sprites were preceded by a cloud-to-ground stroke with a coincident sferic and sky flash. All cloud-to-ground strokes associated with sprites were positive, and most had 100 kA or more inferred peak current. Using the

photometer data, the duration of sky flashes induced by the cloud-to-ground strokes was determined to be ~ 3 ms, and the additional sprite total light curve also endured for ~ 3 ms.

1.6. Observations During Summer 1995

Video images of sprites were obtained by *Rairden and Mende* [1995] with a CCD camera during a July 1995 ground-based campaign near Fort Collins, Colorado. These unfiltered intensified images reveal detailed spatial structure within the sprite envelope. The temporal resolution of the standard interlaced video imagery is limited by the 60 fields per second acquisition rate (16 ms). The specific CCD used here, however, is subject to bright events leaking into the readout registers, allowing time resolution of the order of the linescan rate (63 μ s). Typical sprite onset is found to follow the associated cloud-to-ground lightning by 1.5 to 4 ms. The onsets of the individual sprites within a cluster are generally, but not always, simultaneous to within 1 ms. Sprites tend to have a bright localized core, less than 2 km in horizontal dimension, which rises to peak intensity within 0.3 ms and maintains this level for 5 to 10 ms before fading over an additional 10 ms.

1.7. Spectral, Photometric and Other Properties of Sprites

Spectra of sprites in the stratosphere/mesosphere above electrically active cumulonimbus clouds were acquired on July 16, 1995 from an observation site near Fort Collins, Colorado, by *Mende et al.* [1995]. The spectra, resolved from ~ 450 –800 nm, included four distinct features in the 600–760 nm region which have been identified as the N_2 first positive system with $\Delta=2,3$, and 4 from the $v=2,4,5,6$ vibrational levels of the $B^3\Pi_g$ state. The spectra were lacking in other features such as the N_2^+ Meinel or the N_2^+ first negative system which led the authors [*Mende et al.*, 1995] to a conclusion that the electron energy causing the excitation is quite low. However, with the available signal-to-noise ratio of the measurement, in order to be detectable these other features would have had to be at levels no less than a factor of 10 of that of the N_2 first positive system.

Hampton et al. [1996] used a video slit spectrograph to obtain optical spectra of sprites. Twenty five events were observed from the Mount Evans Observatory over a thunderstorm on the border of Nebraska and Colorado between 0700 and 0900 UT on the night of June 22, 1995. For 10 of these events optical spectra were measured in the wavelength range from 540 to 840 nm. After correcting for the spectrograph response function, digitized spectrograph video images were used to measure the wavelength of, and ratios between, the various emissions. All emissions were found to be those of the first positive bands of N_2 . There was no evidence of the presence Meinel bands of N_2^+ , indicating (in the opinion of the authors) that the mechanism responsible for sprites produces little or no ionization at 70 km altitude. However, it is important to note that, in order to be detectable, the intensity of the Meinel band would

have to be no smaller than a factor of ~ 10 below that of the N_2 first positive band. As we show later (section 3.4), the predicted levels of Meinel band intensities in sprite producing processes which lead to intense ionization are $\sim 10^3$ lower than that of N_2 first positive.

The measurements of both *Hampton et al.* [1996] and *Mende et al.* [1995] are fully consistent with the theoretical results put forth in this paper and are not inconsistent with intense ionization occurring within the luminous regions of sprites. Quantitative interpretation of these results is given in Section 3.4 below.

Recently, spectrally resolved emissions obtained by *Hampton et al.* [1996] and *Mende et al.* [1995] have been analyzed in detail using energy dependent electron excitation cross sections and laboratory data to extract information on the energies of electrons producing the red sprite radiance [*Green et al.*, 1996]. The sprite electrons appear to be of energy sufficient to dissociate and ionize N_2 . There is no clear evidence for the presense of MeV energy electrons as required for runaway breakdown [*Green et al.*, 1996]. Results indicate excitation by electrons with a Boltzmann temperature of 1 eV (range 0.4–2 eV), however, *Green et al.* [1996] suggest that a Druyvesteyn distribution with a suppressed high-energy tail may be more realistic. Thus 1 eV represents a lower bound of characteristic electron temperature [*Green et al.*, 1996].

Sprites are clearly associated both temporally and spatially with intense lightning discharges in underlying thunderstorms [*Boccippio et al.*, 1995] as well as with early/fast VLF events [*Inan et al.*, 1995] providing strong evidence of significant changes in the mesospheric electrical conductivity. Sprites are almost uniquely associated with positive cloud-to-ground lightning discharges [*Boccippio et al.*, 1995; *Winckler et al.*, 1996; *Lyons*, 1996]. The most recent photometric measurements demonstrate that sprites are typically delayed in time ranging from ~ 3 ms [*Winckler et al.*, 1996] to several tens of ms [*Fukunishi et al.*, 1996] with respect to the onset of the causative cloud-to-ground stroke. The duration of sprite events as observed in photometer data usually decays on a time-scale of one video field, although this result may be specific to the spectral range covered by the photometers used.

1.8. Theoretical Mechanisms of Upward Electrodynamic Coupling of Thunderstorms

The new observations listed above have led to the discovery of new interaction mechanisms which result in troposphere-mesosphere/lower ionosphere coupling. These mechanisms are based on heating of the ambient electrons by electromagnetic pulses generated by lightning discharges [*Inan et al.*, 1991, 1996b; *Taranenko et al.*, 1993a, b; *Milikh et al.*, 1995; *Rowland et al.*, 1995, 1996; *Glukhov and Inan*, 1996] or by large quasi-electrostatic thundercloud fields [*Pasko et al.*, 1995, 1996a, b; *Boccippio et al.*, 1995; *Winckler et al.*, 1996] and on runaway electron processes [*Bell et al.*, 1995; *Winckler et al.*, 1996; *Roussel-Dupre and Gurevich*, 1996; *Taranenko and Roussel-Dupre*, 1996; *Lehtinen et*

al., 1996]. It has been proposed by *Inan et al.* [1996d] that quasi-electrostatic thundercloud fields are capable of maintaining the ionospheric electrons at a persistently heated level well above their ambient thermal energy. Changes in the thundercloud charge (e.g., in lightning discharges) lead to heating/cooling above/below this quiescent level and are registered as early/fast VLF events [Inan et al., 1996d]. V. P. Pasko et al. (Ionospheric effects due to electrostatic thundercloud fields, submitted to *Journal of Atmospheric and Terrestrial Physics*, 1996, hereinafter referred to as V. P. Pasko et al., submitted manuscript, 1996) has recently proposed a new model demonstrating that static thundercloud electric fields can also significantly heat lower ionospheric electrons and potentially alter the chemical balance in the *D* region. The simultaneous observations of early/fast VLF events and sprites [Inan et al., 1995] indicate that these two effects may be a manifestation of the same physical process consistent with model predictions of both optical emissions, heating, and ionization changes associated with quasi-electrostatic thundercloud fields [Pasko et al., 1995, 1996a, b; Inan et al., 1996d]. Some of these physical processes are illustrated in Figure 1.

It is important to note that in spite of the modeling efforts of different authors during last several years and the fact that results of the developed models agree with bulk of video, photometric, and spectral measurements of sprites [e.g., Pasko et al., 1996a], the sprite morphology (especially their fine spatial structure and clustering) is still not fully understood. It was suggested by Pasko et al. [1996a] that vertically striated structure of sprites can be a result of development of streamer type channels of breakdown ionization. It was also suggested that clusters of sprites can result from local inhomogeneities in the mesospheric conductivity [Pasko et al., 1996a]. Recently, Rowland et al. [1996] considered the breakdown of the neutral atmosphere by electromagnetic pulses driven by lightning and proposed that modulation of atmospheric neutral density associated with gravity wave motions may contribute to observed spatial modulation of ionization and could generate some of the structure observed in the high-altitude emissions. However, no particular mechanism of gravity wave generation leading to vertically striated structures typical for sprites has yet been identified. Mechanisms of sprites based on acceleration and avalanche of cosmic ray secondary electrons by quasi-electrostatic (QE) fields [e.g., Bell et al., 1995] may naturally explain the vertical structure of sprites, their fast appearance in time, as well as gamma-ray emissions above thunderstorms [Fishman et al., 1994; Inan et al., 1996c; Lehtinen et al., 1996]. Predicted spectra produced by the runaway mechanism should contain intense Meinel and 1st negative bands of N_2^+ [Bell et al., 1995]. The presense of the 1st negative band of N_2^+ (in particular 427.8 nm emission) in sprites has been recently reported [Armstrong et al., 1995]. The ratio of this emission to the 1st and 2nd positive bands of N_2 is yet to be determined. In the event that the conventional heating and

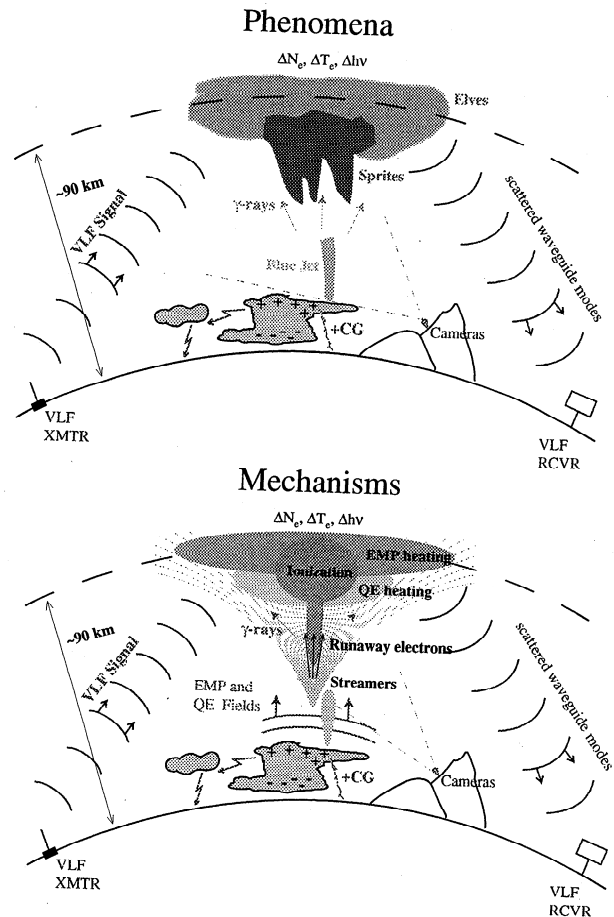


Figure 1. Illustration of different (top) phenomena and (bottom) theoretical mechanisms of lightning-ionosphere interactions operating at different altitudes and producing optical emissions ($\Delta\nu$) observed as sprites, blue jets and elves, as well as heating (ΔT) and ionization changes (ΔN_e) detected as very low frequency (VLF) signal changes.

runaway mechanisms operate simultaneously to create sprites, the altitude profiles of spectral ratios could determine the regions dominated by each mechanism [Bell et al., 1995].

It should be noted that the possibility of breakdown ionization of the upper atmosphere by thundercloud fields was first mentioned by Wilson [1925]. He recognized that the relation between the thundercloud electric field which decreases with altitude z as $\sim z^{-3}$ and the critical breakdown field which falls more rapidly (being proportional to the exponentially decreasing atmospheric density) leads to the result that "there will be a height above which the electric force due to the cloud exceeds the sparking limit" [Wilson, 1925]. In the same paper, Wilson suggested the possibility of accelerated cosmic ray secondary electrons emitting γ -rays above thunderstorms. Three decades later Wilson speculated that a discharge between the top of a cloud and the ionosphere might often be the normal accompaniment of a lightning discharge to ground [Wilson, 1956].

1.9. Purpose of This Paper

The quasi-electrostatic (QE) heating model developed by *Pasko et al.* [1995] after some modifications has been successfully applied to explain many of the observed features of sprites [Bell et al., 1995; Pasko et al., 1996a] and jets [Pasko et al., 1996b], as well as to provide an insight into possible physical effects associated with early/fast VLF events [Inan et al., 1996c]. The purpose of this paper is to provide a detailed description of the QE model [Pasko et al., 1995] and predicted results under a variety of ambient atmospheric/lower ionospheric conditions. For simplicity, in most of our calculations we assume the discharge duration to be ~ 1 ms, similar to Pasko et al. [1995]. We evaluate the electron density changes due to dissociative attachment to O_2 and the impact ionization of O_2 and N_2 and the two-dimensional (2-D) distribution of optical emission intensity (3-D cylindrically symmetric distributions are integrated along the horizontal line of sight to simulate 2-D distribution observed by an imager) of the 1st and 2nd positive bands of N_2 , Meinel and 1st negative bands of N_2^+ , and the 1st negative band of O_2^+ caused by QE heating and ionization in the lower ionosphere. We examine the dependence of the QE heating and ionization upon the altitude profile of ion conductivity, number density of electrons, atmospheric neutral density distribution, and duration of lightning discharge. We also discuss the dependence of QE heating on different types of lightning discharge (i.e., intracloud versus positive or negative cloud-to-ground) as well as on the thundercloud charge geometry. Finally, we analyze the relaxation properties of the electric field in the conducting medium. Results of our model calculations are compared with the results of recent video and spectroscopic observations of sprites.

2. Model Formulation

We base our considerations on the general QE model of ionospheric heating [Pasko et al., 1995], the basic mechanism of which is as follows:

2.1. Physical Mechanism

The mechanism of the penetration of the thundercloud electric fields to the higher-altitude regions is illustrated in Figure 2. As the thundercloud charges slowly build up before a lightning discharge, high-altitude regions are shielded from the quasi-electrostatic fields of the thundercloud charges by space charge induced in the conducting atmosphere at lower altitudes. The appearance of this shielding charge is a consequence of the finite vertical conductivity gradient of the atmosphere above the thundercloud. When one of the thundercloud charges (e.g., the positive one as shown in Figure 2) is quickly removed by a lightning discharge, the remaining charges of opposite sign in and above the thundercloud produce a large quasi-electrostatic field that appears at all altitudes above the thundercloud, and endures for a time equal to approximately (see discussion in section 3.9) the local relaxation time ($\tau_r = \epsilon_0/\sigma$) at each altitude. This large electric field can be thought of as being the difference between the electrostatic field dictated (via Coulomb's law) by the dipole configuration of thundercloud charges and the polarization charge which are in effect before the discharge, and that required by the combination of the single thundercloud charge remaining after the discharge and the polarization charge. These temporarily existing electric fields lead to the heating of ambient electrons and the generation of ionization changes and optical emissions.

In cases of more complex charge distributions in the thundercloud which sometimes involve up to six charge layers in the vertical direction [e.g., Marshall and Rust, 1993], each of the charge centers can be viewed as generating its own polarization charge in and above thundercloud, and the resultant configuration of the electric field and charge density can be obtained by using principle of superposition. This consideration is helpful in visualization of the fact that the electric field appearing at mesospheric altitudes after the charge removal by cloud-to-ground lightning discharge is defined mostly by the absolute value and altitude of the removed charge and is essentially independent of the complexity of the

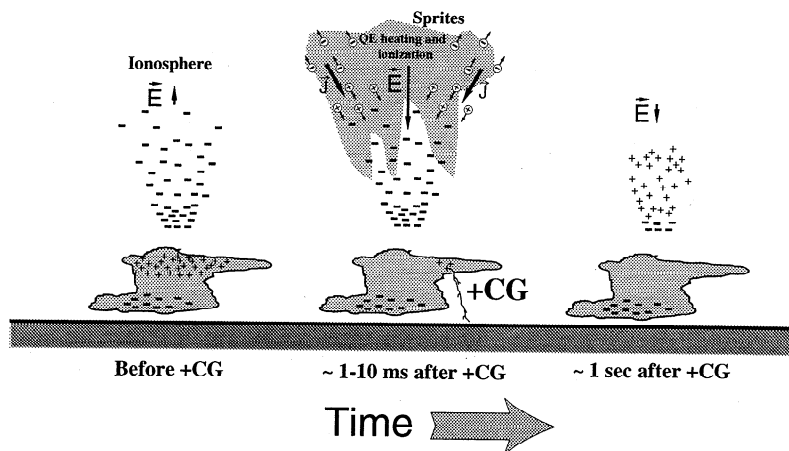


Figure 2. Illustration of the mechanism of penetration of large quasi-electrostatic thundercloud fields to mesospheric altitudes, leading to electron heating, breakdown ionization, and excitation of optical emissions.

charge configuration in the cloud. The charge removal can also be viewed as the “placement” of an identical charge of opposite sign. The initial field above the cloud is simply the free space field due to the “newly placed” charge and its image in the ground which is assumed to be perfectly conducting. This effect will be further illustrated in the context of the results of our calculations (section 3.7).

2.2. Electric Field and Charge Density

The quasi-electrostatic field is established in the mesosphere and lower ionosphere due to the accumulation of thundercloud charge and its evolution in time as a portion of the charge is lowered to the ground by a positive cloud-to-ground (+CG) or negative cloud-to-ground (-CG) lightning stroke, or neutralized inside the cloud due to an intracloud (IC) discharge (Figure 3). In addition, (see section 3.7 for more details) we consider the specific cases of the removal or deposition of monopole charges (see cases marked M1 and M2 in the top panel of Figure 3).

The quasi-electrostatic fields treated in our model are the slowly varying and long enduring electric component of the total electromagnetic field which is generated by the removal of charge from the cloud. Specifically, we leave out the short-duration electromagnetic pulses (EMP) generated primarily by the return stroke currents and which produce bright optical emissions at 80-95 km altitudes emitted in a thin cylindrical (doughnut-like) shell expanding to radial distances up to 150 km [see *Inan et al.*, 1996b, and references therein] and referred to as “elves” [Fukunishi et al., 1996]. In terms of calculations of the quasi-static electric fields this approach appears to be fully sufficient, as was shown by comparing results obtained from the same quasi-static equations used in our model with the results of solutions of a full set of Maxwell equations [Baginski and Hodel, 1994].

Any effects associated with magnetic fields are necessarily left out in our formulation. The effects of the Earth’s magnetic field can be neglected in view of the extremely high collision rates that are in effect even under mild heating conditions (section 3.3). Any magnetic fields generated due to the slow temporal variations of the quasi-static electric fields are too small to have any effect on the electron dynamics. Indeed, simple estima-

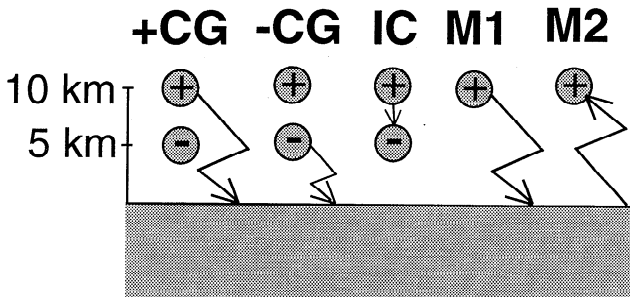


Figure 3. Positive (+CG), negative (-CG), intracloud (IC), monopole removal (M1), and monopole deposition (M2) models of thundercloud “discharges.”

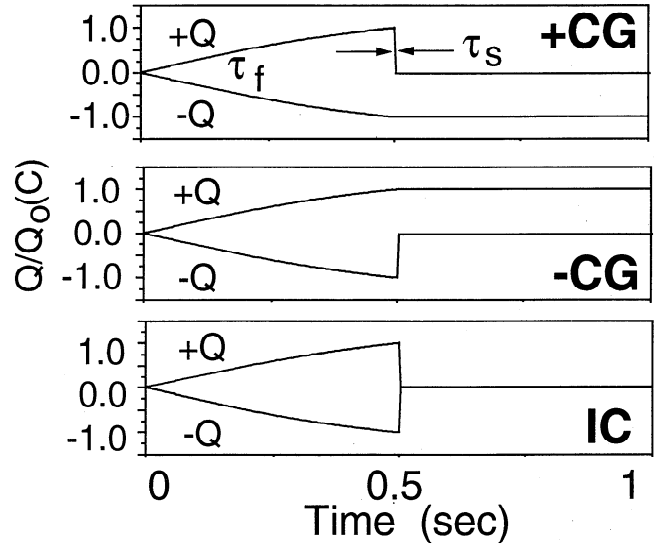


Figure 4. The assumed behavior of the source charges corresponding to +CG, -CG, and IC models.

tions show that the electric field with amplitude ~ 100 V/m which varies on a characteristic time scale ~ 1 ms and has spatial scale ~ 100 km leads to amplitudes of induced magnetic fields which are at least 2 orders of magnitude lower than Earth’s magnetic field and thus can be ignored.

The thundercloud charges $+Q$, $-Q$ form a vertical dipole which is assumed to develop over a time τ_f . The positive or negative charges, or both are then “discharged” (or removed) by decreasing the magnitude of charge with a time constant τ_s , corresponding respectively to +CG, -CG, or IC lightning discharges, as illustrated in Figure 4. Experimental data on lightning discharges indicates that the charge removal time τ_s may vary between ~ 1 ms and several tens of milliseconds [Uman, 1987, pp.124, 196]. In section 3 we concentrate mainly on CG discharges involving relatively rapid removal of charge, namely cases for which $\tau_s \sim 1$ ms. Results for slower discharges are considered in a separate publication [Pasko et al., 1996a].

A cylindrical coordinate system (r, ϕ, z) is used with the z axis representing altitude, as illustrated in Figure 5. The ground and ionospheric boundaries (taken to be at $z=90$ km) are assumed to be perfectly conducting and the entire system is taken to be cylindrically symmetric about the z axis. Two different types of boundary conditions can be utilized at the cylindrical boundary (can be taken, for example, at $r=60$ km). If we assume a perfect conductor at $r=60$ km, we have $\partial\varphi/\partial z = 0$ (or $\varphi = 0$), where φ is the electrostatic potential. This condition was used by Illingworth [1972] and essentially amounts to considering the solution of the electrostatic fields in a “tin can.” Alternatively, we can assume that $\partial\varphi/\partial r = 0$, an assumption adopted by Tzur and Roble [1985]. Both of the boundary conditions are rather artificial and lead to unphysical modification of the electric fields near the boundary. However, the temporal and spatial evolution of the electrostatic

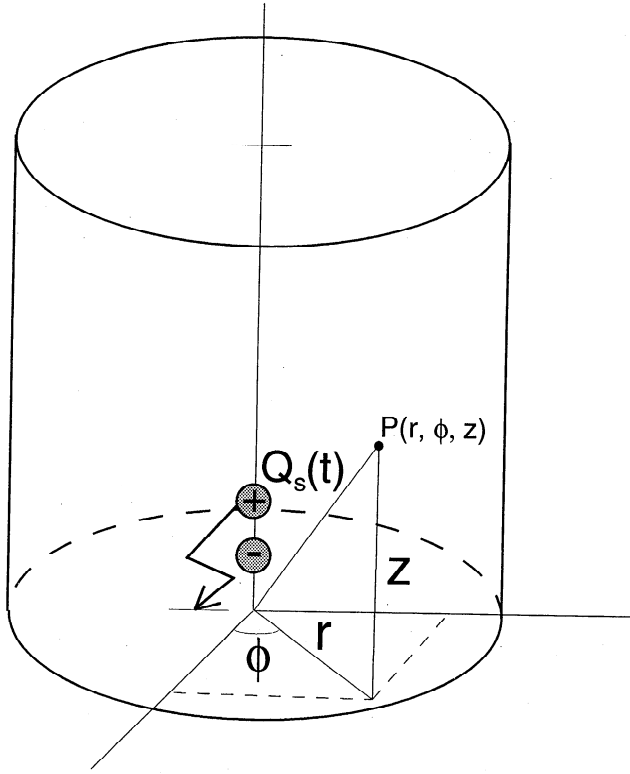


Figure 5. Coordinate system used in calculations.

field system does not depend significantly on these edge fields if the boundaries are chosen to be far enough from the charge sources. The distance $r=60$ km used in our calculations represents a trade off between the resolution which is possible with available computer resources and the accuracy of the electric field calculation. As an example, the presence of the conducting boundary at $r=60$ km leads to an error of less than $\sim 10\%$ on the magnitude of the electric field at $r=50$ km and $z=10$ km.

The electrostatic field \vec{E} , given by $\vec{E} = -\nabla\phi$, the charge density ρ , and the conduction current density $\vec{J} = \sigma\vec{E}$ are calculated using the following system of equations:

$$\frac{\partial(\rho + \rho_s)}{\partial t} + \nabla \cdot (\vec{J} + \vec{J}_s) = 0 \quad (1)$$

$$\nabla \cdot \vec{E} = (\rho + \rho_s)/\epsilon_0 \quad (2)$$

where ρ_s and \vec{J}_s are the thundercloud source charge and current densities which satisfy the equation $\partial\rho_s/\partial t = -\nabla \cdot \vec{J}_s$, where $\nabla \cdot \vec{J}_s = \nabla \cdot \vec{J}_s + \rho_s\sigma/\epsilon_0$, where the effective source current density \vec{J}_s' is introduced so as to compensate any change in the thundercloud charge density ρ_s due to the conduction current. Equation (1) can then be written in the form:

$$\frac{\partial\rho}{\partial t} + \nabla\sigma \cdot \vec{E} + \rho\sigma/\epsilon_0 = 0 \quad (3)$$

If in (1) one simply assumes $\partial\rho_s/\partial t = -\nabla \cdot \vec{J}_s$, (i.e., $\vec{J}_s = \vec{J}_s'$), it is necessary that $\rho\sigma/\epsilon_0$ be substituted with

$(\rho + \rho_s)\sigma/\epsilon_0$. In this case, if one ignores the effects of the conductivity gradients, the quasi-stationary solution of (3) is simply $\rho = -\rho_s$, so that the source charge is completely compensated by charge induced in the conducting medium over a time scale $\sim \epsilon_0/\sigma$. Strictly speaking, ρ_s is a function of time (i.e., $\rho_s = \rho_s(t)$) so that the quasi-stationary solution $\rho = \rho_s$ has physical meaning only in the case when the characteristic timescale of $\rho_s(t)$ is much longer than ϵ_0/σ . As can be seen from (1) and (2), the introduction of \vec{J}_s' allows us to specify the charge dynamics inside the cloud as an externally determined function of time.

Physically, the current \vec{J}_s' as a source of ρ_s is associated with the process of separation of charges inside the cloud and is directed opposite to the resulting electric field [Wilson, 1956]. The current \vec{J}_s' may be related to the small and light positively charged ice splinters, which are driven upward by a strong stream of convecting air, and heavy negatively charged hail particles which are driven downward by gravity [Malan, 1963, p. 76; Uman, 1987, p. 65]. We note that the model of thundercloud charges used in this paper is rather simplified in comparison with the actual vertical distribution of charge density in mesoscale convective systems (MCS) producing sprites, which may sometimes have up to six layers of charge with complicated spatial structure [e.g., Marshall and Rust, 1993; Rust et al., 1996]. However, as we show later, physical results of our model depend mostly on the magnitude and altitude of the charge removed by the cloud-to-ground lightning discharge and are essentially independent of the details of the initial configuration of charges with different polarities in the thundercloud.

We assume that $\rho_s = \rho_+ + \rho_-$ and that the separated dipole charges (i.e., $+Q$ or $-Q$) are represented as distributed charge densities $\rho_+(\vec{r}, t)$ or $\rho_-(\vec{r}, t)$ having a Gaussian spatial distribution given by $\rho_{\pm}(\vec{r}, t) = \rho_0 e^{-[(z-z_{\pm})^2 + r^2]/a^2}$ with $a=3$ km, $z_-=5$ km, $z_+=10$ km, so that the total source charges are $\pm Q(t) = \int \rho_{\pm}(\vec{r}, t) dV$. Our formulation can also be used to consider of horizontally extended charge distributions similar to those existing in mesoscale convective systems [Boccippio et al., 1995; Marshall et al., 1996; E. Williams, private communication, 1994]. In such a case, the charge density corresponding to the thundercloud charges would have a Gaussian distribution in the z direction while being uniform in the r direction, with its scale determined by the radius of the "disk" of charge. This disk charge density is normalized accordingly so that we still have $\pm Q(t) = \int \rho_{\pm}(\vec{r}, t) dV$.

Equation (3) is integrated in time using an explicit two-step method of solution of ordinary differential equations [Potter, 1973, p. 34]. At each time step the electric field \vec{E} to be used in (3) is found by integration of (2) via the method of cyclic reduction [Buneman, 1969] using a FORTRAN routine published by Swartrauber and Sweet [1975]. The conductivity σ in (3) is calculated self-consistently by taking into account the effect of the electric field on the electron component through changes in mobility (due to heating) and electron density (due

to attachment and/or ionization) as discussed in subsequent sections 2.4 and 2.5. A fourth-order Runge-Kutta method and different conservative and nonconservative numerical schemes are also employed to test the accuracy of results obtained.

2.3. Lightning Current and Charge

The important input parameters that need to be specified externally for each model calculation are (1) the altitude profiles of ambient ion conductivity and electron density; (2) the magnitude (Q_o) of the charge transferred (e.g., by a CG lightning discharge) and the time constant (τ_s) which determines the rate at which the charge is transferred; and (3) the altitude of the charge removed. None of these parameters are directly available in a typical experimental context, except for the fact that the National Lightning Detection Network (NLDN) records lightning intensity (or peak current I_p [e.g., *Idone et al.*, 1993]) does imply some restrictions on the magnitude of the removed charge Q and the time-scale of the charge removal τ_s .

In the context of the quasi-electrostatic heating model, the thundercloud charging and discharging process is assumed to consist of two stages. During the predischage stage with duration τ_f , charge Q_o slowly (hundreds of seconds) accumulates in the thundercloud. The second stage is the lightning discharge, during which the thundercloud charge is quickly and completely removed from the thundercloud over a time τ_s , usually of the order of several ms. Mathematically, the continuous thundercloud charge dynamics can be represented in the form:

$$Q(t) = Q_o \frac{\tanh(t/\tau_f)}{\tanh(1)}, \quad 0 < t < \tau_f$$

$$Q(t) = Q_o \left[1 - \frac{\tanh(t/\tau_s)}{\tanh(1)} \right], \quad \tau_f < t < \tau_f + \tau_s$$

$$Q(t) = 0, \quad \tau_f + \tau_s < t$$

Note that the choice of the functional variation as $\tanh(\cdot)$ is rather arbitrary but is not critical for the physics of the phenomena modeled.

For this particular assumed functional dependence of $Q(t)$ the amplitude of the peak current at $t = \tau_f$ can be calculated as

$$I_p = \frac{dQ}{dt} = \frac{Q_o}{\tau \tanh(1)}, \quad t = \tau_f$$

Having calculated I_p , the value of the peak electric field at a distance of 100 km from the lightning discharge can be found as [Orville, 1991]

$$E_{100} = \frac{I_p v}{2\pi D \epsilon_o c^2}$$

where c is speed of light in free space, ϵ_o is dielectric permittivity of free space, $D = 10^5$ m, and $v = 1.5 \times 10^8$ m/s.

For example, $E_{100} = 75$ V/m corresponds in this model to a peak current of $I_p = 270$ kA and a total charge removed in lightning of $Q_o = 200$ C, if we assume $\tau_s = 1$ ms, a reasonable value based on experimental data [Uman, 1987, pp. 124, 199]. We note that the duration of the lightning discharge τ_s as well as the functional time dependence of the charge removal $Q(t)$ as given above are not available from measurements provided by NLDN. Nevertheless, these parameters constitute critically important inputs for modeling the corresponding heating and ionization changes in the lower ionosphere.

Another important input to the model is the ambient ion conductivity profile, which determines the relaxation time for the quasi-electrostatic field and thus the amount and duration of heating for given values of Q_o and τ_s . Detailed description of the conductivity model is given in the following sections.

2.4. Ambient Conditions in the Atmosphere and Lower Ionosphere

For the various model calculations in this paper, we consider three different models of ambient electron number density (Figure 6a). These models of electron density were used in previous studies of subionospheric VLF propagation in the presence of localized ionospheric disturbances caused by lightning induced electron precipitation [e.g., *Pasko and Inan*, 1994]. They were employed in this paper to represent a wide range of possible variability of the electron density in the nighttime lower ionosphere.

For the ambient ion conductivity, we consider three different altitude profiles as illustrated in Figure 6b. For

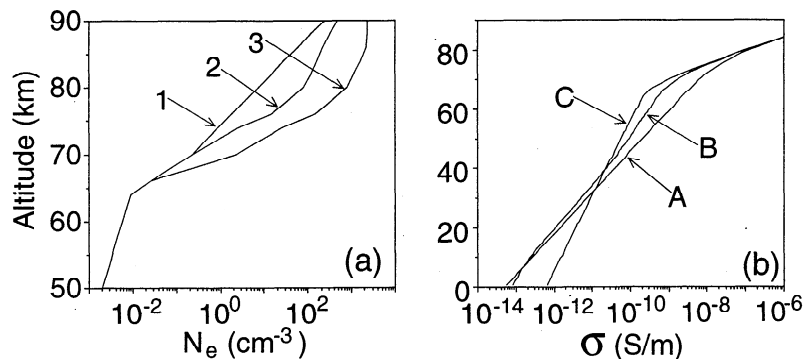


Figure 6. Three altitude profiles of (a) ambient electron number density, and (b) ion conductivity used in the various calculations reported in this paper.

illustrative purposes the ambient conductivity profiles in Figure 6b also include the electron component σ_e which is given by

$$\sigma_e = q_e N_e \mu_e \quad (4)$$

where q_e is the electronic charge, N_e is the number density of electrons, and μ_e is the electron mobility. The electron conductivity σ_e is typically dominant over ion conductivity at altitudes above ~ 60 km. The total conductivity profiles shown in Figure 6b were calculated with the electron component (dominant at >60 km altitude) determined by the electron density profile 1 shown in Figure 6a, and electron mobility for essentially cold electrons of $\mu_e = 1.36 N_o / N \text{ m}^2/\text{V/s}$, where $N_o = 2.688 \times 10^{25} \text{ m}^{-3}$, and N is number density of air molecules (see section 2.5.1 for further details).

At altitudes <60 km, the total conductivity is dominated by the ion conductivity. Profile A ($\sigma_A = 5 \times 10^{-14} e^{z/6\text{km}} \text{ S/m}$, $1 \text{ S} = 1 \text{ mho}$) is taken from [Dejnakarintra and Park, 1974], while Profile C ($\sigma_C = 6 \times 10^{-13} e^{z/11\text{km}} \text{ S/m}$) is derived from experimental measurements of Holzworth *et al.* [1985]. The intermediate profile B is calculated on the basis of the known mobility of ions μ_i as a function of altitude ($\mu_i \sim 2.3 \times 10^{-4} N_o / N \text{ m}^2/\text{V/s}$) [Davies, 1983] and assuming the number density of ions to be $\sim 10^3 \text{ cm}^{-3}$ [Reid *et al.*, 1979]. We note that A, B, and C are used to mark ambient ion conductivity profiles. In further calculations we will use different combinations of ions conductivity profiles (A, B, or C) and electron conductivities defined by the electron density profiles (1, 2, or 3, as shown in Figure 6a).

We neglect the effects of the magnetic field of the Earth on the conductivity since, for the range of parameters considered, the ionospheric plasma is highly collision dominated (see section 3.3 for detailed justification of this assumption).

2.5. Self-consistent Evaluation of Conductivity

In a weakly ionized collisional medium such as the lower ionosphere and the mesosphere, both the electron mobility and the electron density depend nonlinearly on the electric field. The heating of the ambient elec-

trons by the intense fields leads to substantial modification of the atmospheric conductivity at altitudes >60 km. The modified conductivity in turn determines the penetration and relaxation of the electric field, so that it is necessary to self-consistently determine the evolution of the conductivity as we solve for the evolution of the quasi-static field and the associated consequences (e.g., optical emissions). This self-consistent solution is one aspect of our work that was left out in earlier formulations of penetration of thundercloud fields to the ionosphere [e.g., Dejnakarintra and Park, 1974; Baginski *et al.*, 1988], in which the conductivity was simply assumed to remain equal to the assumed ambient profiles. Note that the heating of electrons only modifies conductivity at $>\sim 60$ km altitudes where the electron component of the conductivity is dominant. At altitudes below 60 km, where ions are dominant, the conductivity remains equal to the ambient levels, since the ions are not significantly heated by the electric field.

2.5.1. Electron mobility. The electron mobility μ_e is a complicated function of the electric field as determined by the various loss processes each having different cross sections [see Taranenkov *et al.*, 1993a, b, and references therein]. In this paper, we adopt a functional dependence of μ_e on the magnitude of the electric field E which is derived from experimental data [Davies, 1983; Hegerberg and Reid, 1980]. This function is shown in Figure 7 and can be expressed in the following analytical form:

$$\log(\mu_e N) = \sum_{i=0}^2 a_i x^i, \quad EN_o/N \geq 1.62 \times 10^3 \text{ V/m} \quad (5)$$

$$\mu_e N = 1.36 N_o, \quad EN_o/N < 1.62 \times 10^3 \text{ V/m}$$

where $x = \log(E/N)$, $a_0 = 50.970$, $a_1 = 3.0260$, and $a_2 = 8.4733 \times 10^{-2}$. The analytical expression (5) can be used for computationally efficient calculation of the electron mobility for any combination of electric field and number density of air molecules (i.e., altitude). This analytical method provides results which compare well with those obtained from fully kinetic formulations, as discussed in further detail in Appendix A.

Another parameter which is often useful in specifying

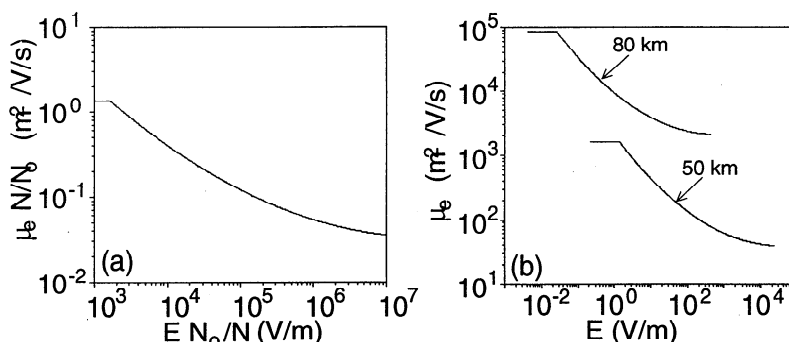


Figure 7. (a) The electron mobility μ_e is shown as a function of the electric field E and the molecular number density N of atmospheric gas; (b) unnormalized μ_e is shown at two selected altitudes (50 and 80 km).

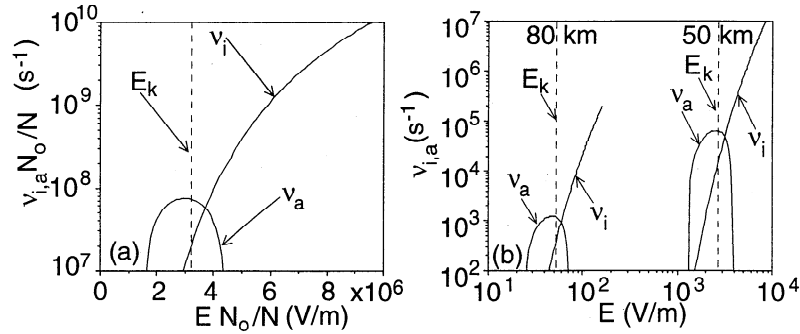


Figure 8. (a) The ionization ν_i and dissociative attachment ν_a coefficients are shown as a function of the electric field E and the molecular number density N of the atmospheric gas; (b) unnormalized ν_i and ν_a are shown at two selected altitudes (50 and 80 km).

the degree of electron heating is the effective frequency of electron collisions with ambient neutral gas. This parameter, denoted ν_{eff} , is given as a simple function of the electron mobility μ_e as $\nu_{\text{eff}} = q_e/(\mu_e m_e)$.

2.5.2. Ionization coefficient. In addition to the nonlinear dependence of μ_e on E , the local value of the electron density N_e depends highly nonlinearly on the electric field due to impact ionization and dissociative attachment processes. These processes begin to become significant as the electric field exceeds a certain threshold and eventually lead to “dielectric breakdown” of the atmospheric gas.

For quantitative description of atmospheric and ionospheric air breakdown we use the ionization coefficient ν_i given by Gurevich *et al.* [1978] and Papadopoulos *et al.* [1993], which for our quasi-static case ($\omega \rightarrow 0$, where ω is the angular frequency with which the electric field is assumed to vary) is illustrated in Figure 8 and which can be expressed in the following analytical form [Papadopoulos *et al.*, 1993]:

$$\nu_i = 7.6 \times 10^{-13} N x^2 f(x) e^{-4.7(1/x-1)}, \quad (6)$$

where

$$f(x) = \frac{1 + 6.3e^{-2.6/x}}{1.5}$$

$x = E/E_k$, and $E_k = 3.2 \times 10^6 N/N_o$ V/m is the characteristic air breakdown field shown for reference in Figure 8 by a dashed line.

It should be noted that due to the relatively slow variation of the electric field the conductivity in our model is assumed to be independent of frequency. Similarly, the ionization coefficient, although originally derived for radio frequency (RF) fields of certain definable frequency ω [Papadopoulos *et al.*, 1993], is used in this paper to be in DC limit ($\omega \rightarrow 0$). Both assumptions are well justified since for quasi-static electric fields $\omega < \sim 10^3$ rad/s and always remains much less than ν_{eff} and frequencies in RF range [Papadopoulos *et al.*, 1993].

2.5.3. Attachment coefficient. In our quasi-electrostatic heating formulation, we can include the two-body attachment of electrons to O_2 molecules with dissociation ($e^- + O_2 \rightarrow O + O^-$). The effective coefficient ν_a

of this reaction is shown in Figure 8 and is a function of electric field which is derived from experimental data [Davies, 1983]. This quantity can be expressed in the following analytical form:

$$\nu_a = \frac{N}{N_o} \sum_{i=0}^2 a_i x^i \quad (7)$$

where $x = EN_o/N$, $a_0 = -2.41 \times 10^8$, $a_1 = 211.92$, and $a_2 = -3.545 \times 10^{-5}$. The attachment coefficient ν_a given in (7) is an effective coefficient which is a function of the true attachment coefficient (for O^- formation), the charge transfer coefficient, and the detachment coefficient [Davies, 1983].

At very low values of ν_i and ν_a (in the region of electric fields $E < E_k$) the value of the attachment coefficient ν_a as given by (7) becomes smaller than the ionization coefficient ν_i as given by (6) and leads to unphysical results. For such low values of $\nu_a N_o/N$, which correspond to $EN_o/N < 1.628 \times 10^6$ V/m, the value of the attachment coefficient can be found from kinetic calculations [Taranenko *et al.*, 1993b] as

$$\log\left(\frac{\nu_a N_o}{N}\right) = \sum_{i=0}^3 a_i x^i \quad (8)$$

where $x = \log(EN_o/N)$, and the series of coefficients $a_0 = -1073.8$, $a_1 = 465.99$, $a_2 = -66.867$, and $a_3 = 3.1970$ (see also Appendix A).

In previous work on swarm experiments [Davies, 1983] it was recognized that the role of dissociative attachment of electrons to O_2 (the fastest process of loss of electrons under heated conditions which may lead to significant modifications of the lower ionosphere [Taranenko *et al.*, 1993a; Inan *et al.*, 1996b]) is difficult to assess since the measured rates for associative detachment and for collisional detachment are known only within one to three orders of magnitude, respectively. A detailed discussion of the importance of the detachment processes in the analysis of swarm experiments is given by Wen and Wetzer, [1988].

2.5.4. Electron density. The ionization ν_i (equation (6)) and attachment ν_a (equations (7) and (8)) coeffi-

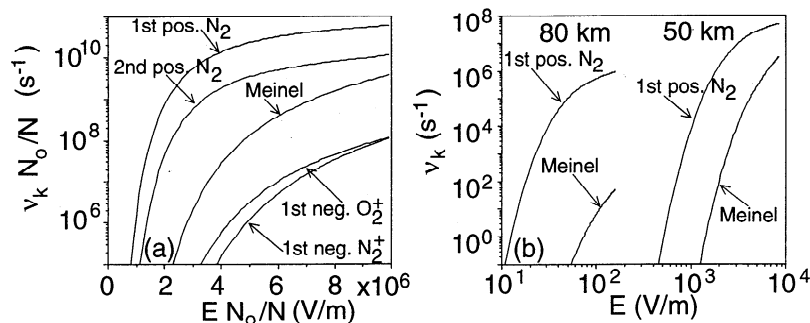


Figure 9. (a) The excitation coefficients ν_k of different optical bands are shown as a function of electric field E and molecular number density N of atmospheric gas; (b) unnormalized ν_k are shown for two selected optical bands (1st positive N₂ and Meinel N₂⁺) and at two selected altitudes (50 and 80 km).

cients are used to calculate the temporal dynamics of the electron density using

$$\frac{dN_e}{dt} = (\nu_i - \nu_a)N_e \quad (9)$$

In summary, in (1) the conductivity σ is calculated as a sum of the ambient ion component σ_i which remains constant in time and the electron component σ_e (4) which is calculated self-consistently by taking into account the effects of the electric field through changes in mobility μ_e (5) due to heating, and changes in the number density of electrons N_e (equation (9)) due to ionization and attachment processes.

2.6. Optical Emissions

Once the temporal and spatial evolution of the electric field is determined via the self-consistent solution of (1) and (2), the intensities of the various optical emissions are determined on the basis of kinetic solutions for the electron distribution function and the excitation coefficients of particular bands. We consider optical emissions from the 1st ($B^3\Pi_g \rightarrow A^3\Sigma_u$) and 2nd ($C^3\Pi_u \rightarrow B^3\Pi_g$) positive bands of N₂, the Meinel ($A^2\Pi \rightarrow X^2\Sigma_g^+$) and 1st negative bands of N₂⁺ ($B^2\Sigma_u^+ \rightarrow X^2\Sigma_g^+$), and the 1st negative band of O₂⁺ ($b^4\Sigma_g^- \rightarrow a^4\Pi_u$) which have short lifetimes and are expected to produce the most intense optical output during impulsive heating of the lower ionospheric electrons [Tararenko et al., 1993a, b].

Analysis of the excitation coefficients ν_k corresponding to these bands obtained from kinetic calculations [Tararenko et al., 1993a, b] for a series of electric field values and air densities shows that relatively simple and accurate analytical approximations similar to those developed for the electron mobility (equation (5)), ionization (equation (6)) and attachment (equations (7) and (8)) coefficients can be derived (see Appendix A). The results are shown in Figure 9 and for the optical bands considered can be expressed in a general form:

$$\log\left(\frac{\nu_k N_0}{N}\right) = \sum_{i=0}^3 a_i x^i \quad (10)$$

where $x = \log(EN_0/N)$, and the series of coefficients a_0, a_1, a_2, a_3 corresponding to the different optical bands are given in Table 1.

The intensity of each optical line in Rayleighs is given by the expression [Chamberlain, 1978, p. 213]:

$$I_k = 10^{-6} \int_L A_k n_k dl, \quad (11)$$

where n_k is the number density of excited particles in state k , A_k is the radiation transition rate, and the integral is taken along L , representing the horizontal line of sight. Our calculations in this paper, do not take into account the effects of radiative transfer between the altitude of the emission and the ground which might be important for the interpretation of the total intensity of optical emissions and their fine spectral features (e.g., the strong attenuation of the (3,1) component of the first positive band of N₂ due to the absorption by O₂ at 762 nm over slant paths [Mende et al., 1995; Hampton et al., 1996]). The blue portion of the visible spectrum can be significantly attenuated due to the Rayleigh scattering, in a manner sensitively dependent on aerosol loading and look angle [e.g., Green et al., 1996].

The quantity n_k is governed by the relation [Sipler and Biondi, 1972]:

$$\frac{\partial n_k}{\partial t} = -\frac{n_k}{\tau_k} + \sum_m n_m A_m + \nu_k N_e \quad (12)$$

where $\tau_k = [A_k + \alpha_1 N_{N_2} + \alpha_2 N_{O_2}]^{-1}$ is the total lifetime of state k , α_1 and α_2 are the quenching rates due to col-

Table 1. Approximation Coefficients

Band	a_0	a_1	a_2	a_3
1st positive N ₂	-1301.0	563.03	-80.715	3.8647
2nd positive N ₂	-1877.1	814.70	-117.46	5.6554
1st negative N ₂ ⁺	-1760.0	724.7	-99.549	4.5862
1st negative O ₂ ⁺	-1802.4	750.91	-104.28	4.8508
Meinel N ₂ ⁺	-2061.1	870.25	-122.43	5.7668

lisions with N_2 and O_2 molecules, respectively, N_{N_2} and N_{O_2} are the number densities of N_2 and O_2 molecules respectively, and the sum over the terms $n_m A_m$ represents increases in n_k resulting from cascading from higher-energy states.

The intensity of the optical bands in (11) is obtained from the number of excited molecules in the upper state n_k which is given by (12). In (12) the electron number density N_e and the excitation coefficients ν_k are the variables which evolve in time and give rise to the optical emissions, and are calculated as functions of the electric field using (9) and (10), as previously described.

The optical emissions from the 1st and 2nd positive bands of N_2 , the Meinel and 1st negative bands of N_2^+ , and the 1st negative band of O_2^+ have the transition rates $1.7 \times 10^5/s$, $2 \times 10^7/s$, $7 \times 10^4/s$, $1.4 \times 10^7/s$, and $8.5 \times 10^5/s$, respectively [Valence-Jones, 1974, p. 119]. Quenching of the 1st positive band emissions occurs primarily through collisions with N_2 molecules, with $\alpha_1 = 10^{-11} \text{ cm}^3/s$ [Valence-Jones, 1974, p. 119]. Quenching of the 2nd positive band occurs primarily through collisions with O_2 molecules with $\alpha_2 = 3 \times 10^{-10} \text{ cm}^3/s$ [Valence-Jones, 1974, p. 119]. For the quenching of the Meinel and 1st negative bands of N_2^+ we have $\alpha_1 = 5 \times 10^{-10} \text{ cm}^3/s$ and $\alpha_1 = 4 \times 10^{-10} \text{ cm}^3/s$, respectively, and for the 1st negative band of O_2^+ we have $\alpha_1 = 2 \times 10^{-10} \text{ cm}^3/s$ [Valence-Jones, 1974, p. 119].

2.7. Limitations of Analytical Models

The simple expressions for mobility (equation (5)), ionization (equation (6)), attachment (equations (7) and (8)), and optical excitation (equation (10)) coefficients are supported by experimental measurements as well as by results of kinetic simulations (see Appendix A for details). These analytical expressions are useful from a computational point of view since they provide fast and reasonably accurate solutions for a wide range of input parameters. However, these models are only valid only for $EN_o/N < 1.6 \times 10^7 \text{ V/m}$ since for fields above this value the mean electron energy approaches the ionization energy and the ionization process becomes nonstationary [see Papadopoulos *et al.*, 1993, and references therein]. The criteria $EN_o/N < 1.6 \times 10^7 \text{ V/m}$ is equivalent to the condition $E/E_k < 5$ given by Papadopoulos *et al.* [1993]. At 70 km altitude, this criteria requires that $E < 1200 \text{ V/m}$, a condition comfortably satisfied for all the cases considered in this work. In addition, the above expressions cannot be used on timescales less than $\sim 10 \mu s$ (this estimate is valid for altitudes $\sim 80\text{--}90 \text{ km}$) which is the time required for the establishment of the stationary electron distribution function [Taranenko *et al.*, 1993a].

3. Results and Discussion

3.1. Model Parameters

In most of the calculations in section 3 we assume the lightning discharge duration to be $\sim 1 \text{ ms}$. We evaluate the electron density changes due to the dissociative attachment of electrons to O_2 and the impact ionization

of O_2 and N_2 , as well as the dynamics and the two-dimensional distribution of the optical emission intensity of the 1st and 2nd positive bands of N_2 , Meinel and 1st negative bands of N_2^+ , and the 1st negative band of O_2^+ , caused by quasi-electrostatic heating and ionization in the lower ionosphere. We examine the dependence of the heating and ionization upon the altitude profile of ion conductivity and the number density of electrons. Some effects associated with the duration of the lightning discharge are also discussed here, although more detailed discussion of this subject is provided by Pasko *et al.* [1996a]. We also discuss the dependence of the quasi-electrostatic heating on the lightning discharge type (i.e., intracloud versus positive or negative cloud to ground) as well as on the thundercloud charge geometry. Finally, we analyze the relaxation properties of the electric field in the conducting medium.

In all of the calculations leading to the results presented below in sections 3.2, 3.3, and 3.4, we use the ambient electron density profile 1 (Figure 6a), the ambient ion conductivity profile A (Figure 6b), and a lightning discharge duration of $\tau_s = 1 \text{ ms}$. In these sections we consider the +CG type of lightning discharge (see Figures 3 and 4). In sections 3.2, 3.3, and 3.4, the distribution of thundercloud charges is assumed to be spherically symmetric and Gaussian with a spatial scale $a = 3 \text{ km}$. The effects produced for different values of above mentioned parameters are investigated in sections 3.5 through 3.8. In all cases, we assume that the thundercloud charge is removed by a lightning discharge from 10 km altitude. Results obtained for given charge values at 10 km altitude are valid for different combinations of charge value and altitude as long as the total thundercloud dipole moment is kept constant. From this point of view, the variation of the altitude of the charge is equivalent (in terms of the resultant physical effects) to the variation of the value of charge at a given altitude, and vice versa. For instance, a 100 C charge removed from 10 km altitude produces approximately the same effects in the lower ionosphere as a 50 C charge removed from 20 km altitude.

3.2. Electric Field and Charge Density

Figures 10 and 11 show the results of model calculations for the case of dipole thundercloud charges of $\pm 200 \text{ C}$. These results are similar to the monopole case considered by Pasko *et al.* [1995] and marked M1 in Figure 3. The slow ($\tau_f = 0.5 \text{ s}$) build-up of the charges leads to the formation of small but finite quiescent quasi-electrostatic fields, which are similar in nature to the fair weather electric field produced by the charges maintained on the Earth [e.g., Uman, 1974; Ogawa, 1985]. The removal of a positive charge in $\tau_s = 1 \text{ ms}$ leads to the appearance of electric fields of up to $\sim 100 \text{ V/m}$ at ionospheric altitudes. Figure 11 shows the spatial distribution of the charge density ρ and the electric field \vec{E} just before ($t = 0.5 \text{ s}$) and right after ($t = 0.501 \text{ s}$) the cloud-to-ground lightning discharge and at $t = 1 \text{ s}$. The physical causes of the "explosive" appearance of the electric field at higher altitudes at $t = 0.501 \text{ s}$ (as

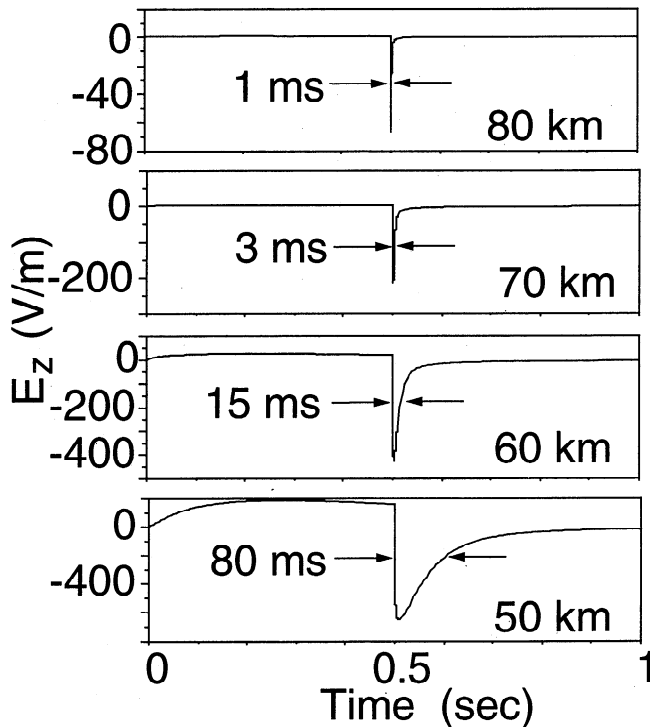


Figure 10. The establishment and relaxation of the z component of the electric field at various altitudes at $r=0$ km for the +CG and M1 models of charge removal (see Figures 3 and 4).

already briefly discussed in section 2.1) can be understood as follows:

As the thundercloud charges accumulate before the lightning discharge, free charges in the mesosphere and lower ionosphere redistribute (Figure 11, top left) to create an electric field \vec{E} approximately equal and opposite to the “applied” electric field \vec{E} due to the large thundercloud charges. Once the thundercloud charge of any polarity is removed, only the electric field \vec{E} due to the charge remaining in thundercloud and the space charge above it remains, and this large field endures for a time determined approximately (see discussion in section 3.9) by the local relaxation time ($\tau_r = \epsilon_0/\sigma$) at each altitude. As we discussed in section 2.1, since charge removal can alternately be viewed as the “placement” of an identical charge of opposite sign, the initial field at ionospheric altitudes is approximately the free space field due to the “newly placed” charge and its image in the ground. Thus the important physical consequences depend primarily on the magnitude and altitude of the removed charge and are essentially independent of the configuration of all other charges in the system. In this regard we note that +CG and M1 models of charge removal (Figure 3) lead to essentially the same electric fields at ionospheric altitudes as is discussed further in section 3.7.

From Figures 10 and 11 the peak electric field at altitude 70 km can be estimated as ~ 200 V/m in good agreement with electric field values required to match

the electron energy distributions which are consistent with the spectral observations of sprites [Green *et al.*, 1996]. The average energy of the electron distribution for $E \sim 200$ V/m at altitude 70 km can be estimated using the analytical expression derived in section A5 as ~ 2.5 eV ($EN_0/N \simeq 2.7 \times 10^6$ V/m at 70 km altitude), also in agreement with the 1 eV lower bound for electron temperature derived by Green *et al.* [1996] assuming a Boltzmann distribution.

3.3. Ionization and Attachment

Figure 12 shows the altitude profile of electron density N_e and the conductivity σ for different values of removed thundercloud charge Q ($Q=50, 100, 150, 200$, and 250 C) at the termination of a lightning discharge ($t=1$ ms). Corresponding profiles of effective electron

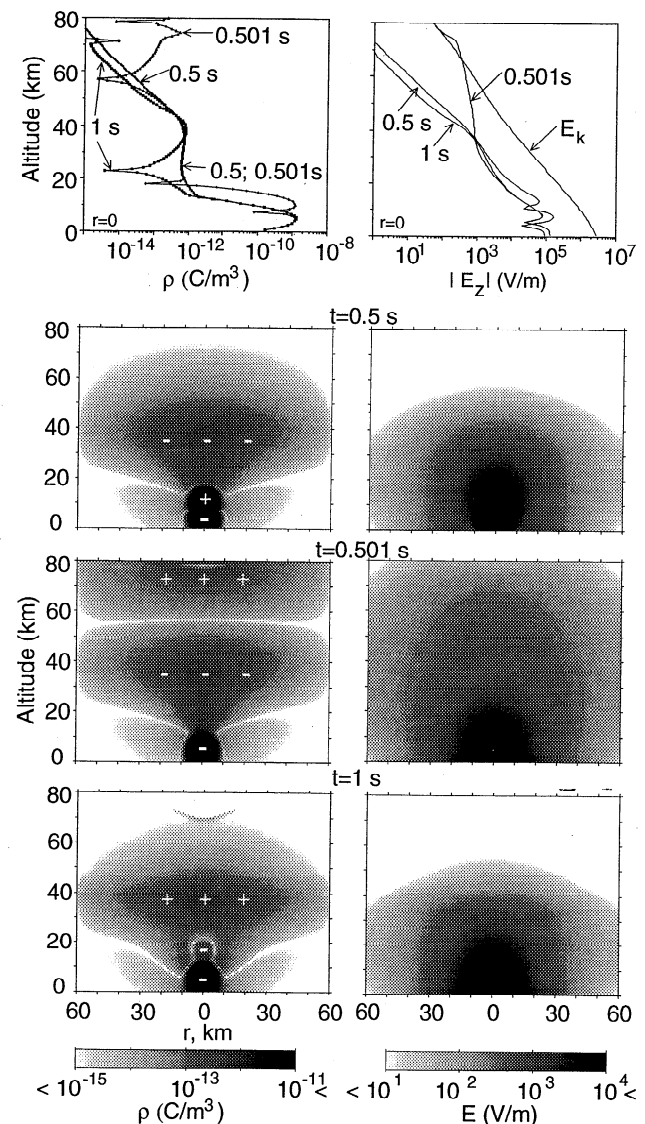


Figure 11. A cross-sectional view of the distribution of the absolute values of the (left) charge density ρ and the (right) total electric field E at selected instants of time. The top panels show altitude scans at $r=0$.

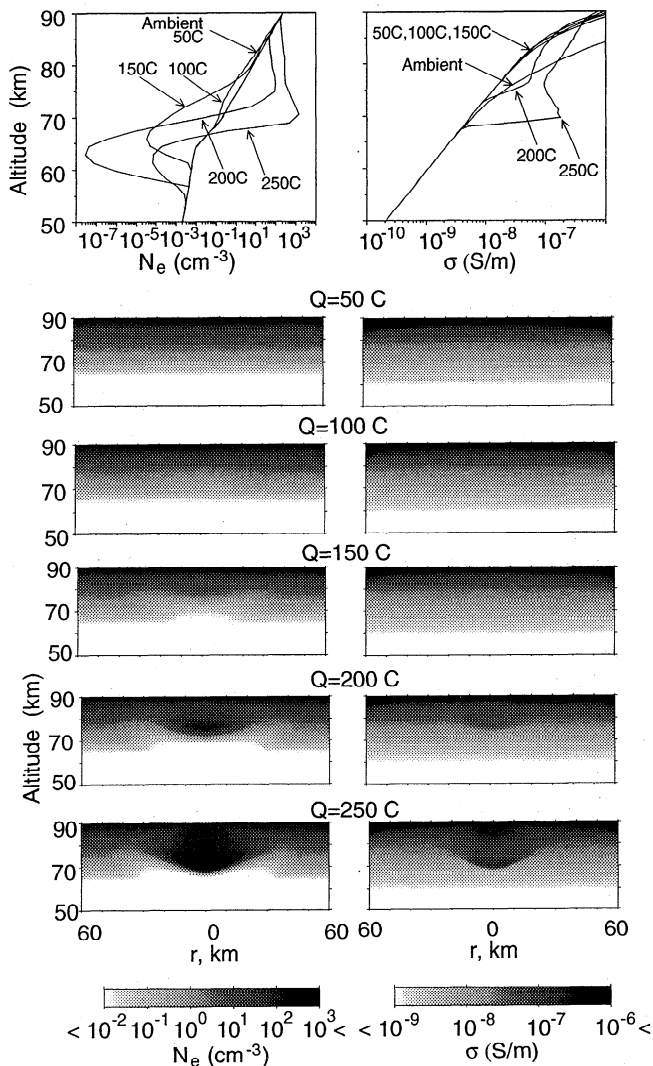


Figure 12. The altitude distribution of the electron density N_e and conductivity σ for different values of thundercloud charge Q at the moment of time $t=1$ ms. The top panels show altitude scans at $r=0$.

collision frequency ν_{eff} , which provides a measure of electron heating, are shown in Figure 13.

During the charge accumulation stage prior to the lightning discharge, the electric field remains below the critical breakdown field E_k (see section 2.5.2) everywhere above the thundercloud (Figure 11 top right). However, the large electric field which appears after the removal of the charge exceeds the breakdown threshold E_k above ~ 70 km altitude, leading to intense ionization changes in the lower ionosphere (Figure 12) and optical emissions (Figure 17).

For higher values of the removed thundercloud charge Q we see from Figure 12 a transition from a regime in which attachment dominates leading to electron density decreases of several orders of magnitude below ambient values to an ionization regime in which dramatic increases in electron density occur. For low Q values such as 50 C (Figure 12) the attachment and ioniza-

tion thresholds are not reached, but nevertheless a large change in effective electron collision frequency occurs (Figure 13), indicating significant changes in electron conductivity (and thus the total conductivity at altitudes > 60 km) purely due to the heating of the electrons.

The changes in the electron density N_e result in corresponding changes in conductivity σ (right-hand panels in Figure 12), although the resultant conductivity changes are determined by the interplay between changes in electron density N_e (due to ionization and attachment) and electron mobility μ_e (due to heating) (equation (4)). For example, the factor of ~ 10 lower conductivity at ~ 80 km altitude for $Q=200$ C versus 100 C is dominantly due to electron heating, since the electron density changes are relatively small.

The altitude scan of the effective electron collision frequency ν_{eff} , modified by heating, is shown in Figure 13 for the same thundercloud charge values as in Figure 12. For purposes of comparison, the electron gyrofrequency is shown in Figure 13 by a vertical dashed line. We note that $\nu_{\text{eff}} > \omega_H$ below ~ 87 km altitude for all charge values considered here. Our assumption concerning the neglect of the effects associated with the external geomagnetic field (section 2.2) is justified since the most important region of the optical emissions associated with sprites is well below this altitude (see section 3.4).

The results in Figure 12 indicate that quasi-electrostatic fields can significantly change the mesospheric/lower ionospheric electron density N_e and conductivity σ at ~ 50 to 90 km altitudes and in regions with ~ 50 -60 km transverse extent. One of the manifestations of such conductivity changes in experimental data may be some early/fast VLF signal perturbations observed in association with lightning discharges and sprites [Inan *et al.*, 1988, 1993, 1995, 1996a].

Often the time period between consecutive discharges from thunderstorm centers [see Uman, 1987, p. 19] is much less than the typical D region relaxation time for

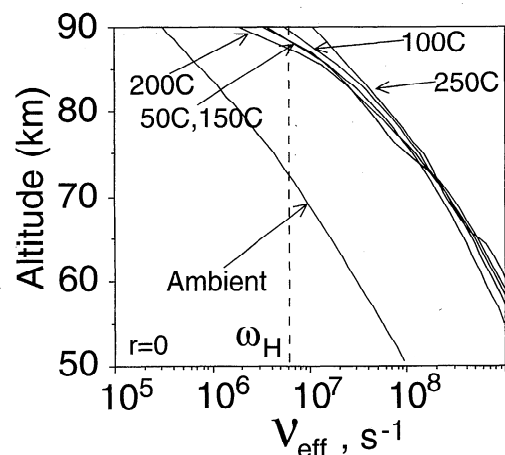


Figure 13. The effective electron collision frequency ν_{eff} is shown as function of altitude for the same thundercloud charge values as in Figure 11. Time $t=1$ ms.

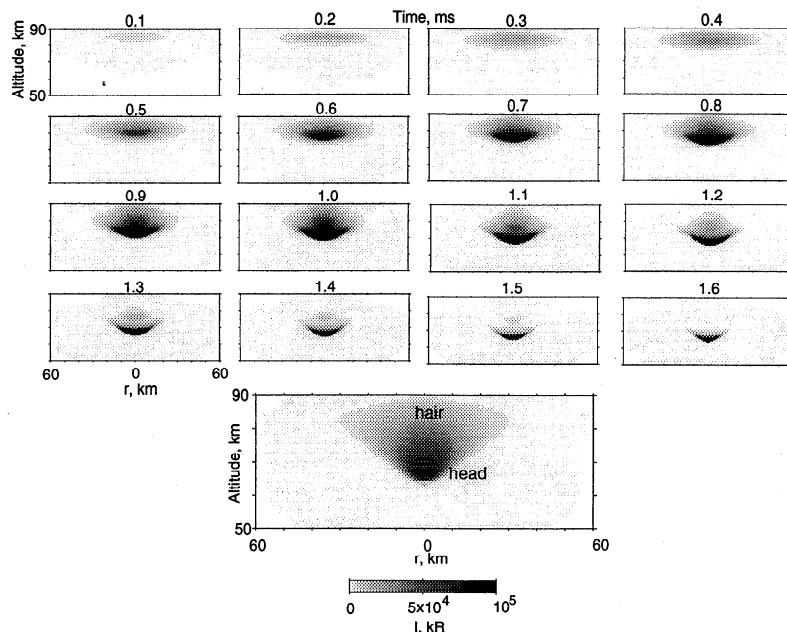


Figure 14. The distribution of intensities (in units of Rayleighs) of emissions of the 1st positive band of N_2 as a function of time for the case of 250 C charge removed from altitude 10 km in 1 ms. The bottom panel shows the corresponding quantities averaged over a time of 1.6 ms.

electron density enhancements (10 to 100 s [e.g., *Pasko and Inan, 1994*]). In such cases quasi-electrostatic fields associated with successive lightning discharges as well as electromagnetic pulses (EMP) generated by lightning strokes can lead to accumulation of the ionization or depletion of the electron density in the lower ionosphere leading to the build up of ionization “bubbles” or attachment “holes” above thunderstorms. Such an effect was predicted by *Inan et al. [1991]* and also discussed by *Taranenko [1993]* in relation to heating and ionization produced by electromagnetic impulses generated by lightning.

3.4. Optical Emissions

The dynamics of the spatial distribution of optical emissions is shown in Figure 14 for $Q = 250$ C. The local optical emissivities of the first (red) positive band of N_2 excited via impact excitation at different points in a cylindrically symmetric volume were integrated along the horizontal line of sight to determine the emission intensities in Rayleighs observed when viewed horizontally from a distant point.

For direct comparison with video observations of sprites [*Sentman et al., 1995*] the optical emissions are averaged over the total duration of sprite luminosity (~ 1.6 ms), which in this case is substantially less than the duration of one video field (~ 16 ms). Results of the averaging are shown in the bottom two panels and are in good agreement with observations of the top part (“head” and “hair” [*Sentman et al., 1995*]) of the sprites. Following the occurrence of the cloud-to-ground discharge, the optical emission initially starts at high altitudes and then moves down, its motion being controlled by the development of ionization and the rela-

tively more rapid relaxation of the electric field at higher altitudes. We note that since the total duration of the optical emission in this case is approximately one-tenth the duration of one video field, the maximum intensity of $\sim 10^5$ kR corresponds to $\sim 10^4$ kR when averaged over a 16 ms field, a value larger than the maximum reported intensity (~ 500 kR) of sprites [*Sentman et al., 1995*] by a factor ~ 10 -100 when viewed through the center of the heated region (at ~ 70 km). This apparent discrepancy is likely due to the response of the optical instruments used to observe sprites as discussed below.

It is important to note that the optical excitation rates for selected bands (i.e., 1st positive band of N_2) are calculated using integral cross sections which do not provide information about the particular wavelength of emitted photons [*Taranenko, 1993*]. Typical color video cameras have well defined red, green, and blue filters [e.g., *Wescott et al., 1995a*] (an example is shown in top left corner of Figure 15) which extract only a narrow part of the spectrum in the visible range of wavelengths. To determine the number of photons corresponding to the 1st positive band of N_2 which produces, for example, the red response of the video camera, one needs to integrate the normalized distribution of emissions in different wavelengths over the band corresponding to the red filter. This consideration is important since most of the energy of the N_2 1st positive band is distributed in the infrared region of the spectrum with only a small fraction in the visible region covered by the red video filter.

The distribution of the intensities as a function of wavelength within all of the different optical bands corresponding to sprites is not yet known. However, on the basis of the first spectral observations of the 1st posi-

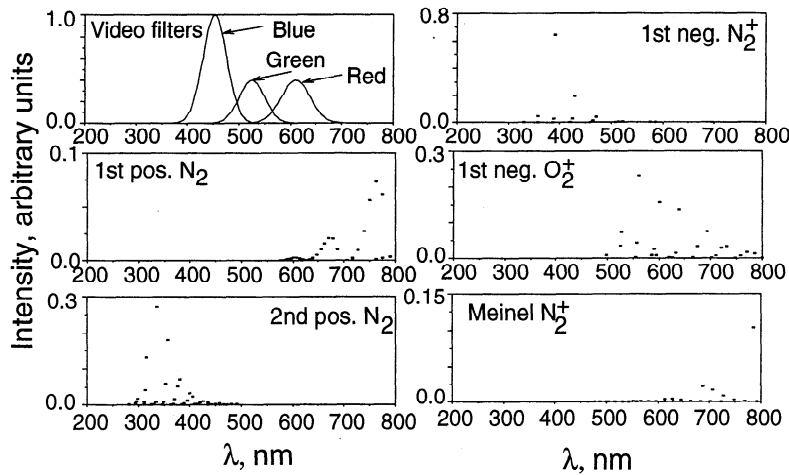


Figure 15. Normalized (to unity) distribution of optical emission intensity as a function of wavelength (assumed to be the same as in aurora) corresponding to different optical bands. Top left corner shows typical red, green, and blue video filters.

tive band of N_2 associated with sprites [Mende *et al.*, 1995; Hampton *et al.*, 1996] (see also section 1.7) the distribution of intensities of the different wavelengths within this band appear similar to that observed in auroral emissions [Valance Jones, 1974, pp.129-132,139] (Figure 15). Although the wavelength distribution for the various components of other emission bands is not yet known, we assume in our further calculations below that the distribution within these bands to be also similar to that in aurorae. Calculations based on this assumption indicate the N_2 1st and 2nd positive bands produce the largest (in comparison with other optical bands) red and blue video response, respectively. Only 1% of the total number of emitted photons corresponding to the N_2 1st positive band appear in the pass band of the red filter of a typical color video camera. The corresponding scaling factor for the predominantly blue N_2 2nd positive band is 2.9%. On the basis of these estimates the optical intensities shown in Figure 14 are in good agreement with video observations of sprites [Sentman *et al.*, 1995]. Scaling factors for selected optical bands and different colors calculated on the basis of video filter responses given by Wescott *et al.* [1995a] are summarized in Table 2. These scaling factors are provided here for illustrative purposes to stress the importance of this type of scaling for the interpretation of the experimental video data, and may be different for

video cameras with different technical characteristics. Furthermore, the scaling factors may strongly depend on the assumption on the auroral-like distribution of optical emissions as a function of wavelength within the bands considered.

Figure 16 shows the results of time averaging of the optical emission intensity of the N_2 1st positive band for different values of removed thundercloud charge. Values of the maximum intensity of the first positive band corresponding to $Q=250, 200, 150, 100, 50$ C are 10^5 kR, 10^4 kR, 10^3 kR, 100 kR, 2 kR, respectively, demonstrating a highly nonlinear dependence of the peak intensity on the removed charge value Q , as expected on the basis of the threshold-like behavior of the optical excitation cross sections. This result is also consistent with the experimental fact that sprites are associated with only

Table 2. Video Response Scaling Factors

Band	Red	Green	Blue
1st positive N_2	1.04×10^{-2}	9.23×10^{-5}	5.65×10^{-10}
2nd positive N_2	7.10×10^{-8}	3.17×10^{-4}	2.86×10^{-2}
1st negative N_2^+	3.60×10^{-4}	5.10×10^{-3}	1.80×10^{-1}
1st negative O_2^+	1.30×10^{-1}	8.60×10^{-2}	1.90×10^{-3}
Meinel N_2^+	3.80×10^{-3}	3.63×10^{-4}	4.56×10^{-5}

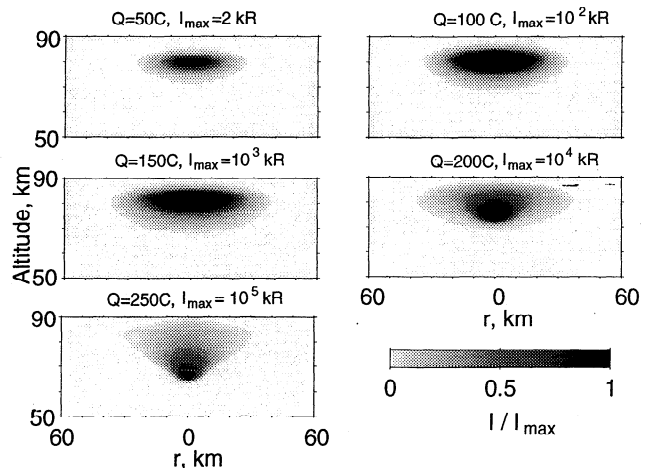


Figure 16. The distribution of the time-averaged intensity (in units of Rayleighs) of emissions of the 1st positive band of N_2 is shown on linear scale and for different values of removed thundercloud charge. It was assumed in all cases that the charge was removed by a lightning discharge from 10 km altitude in 1 ms.

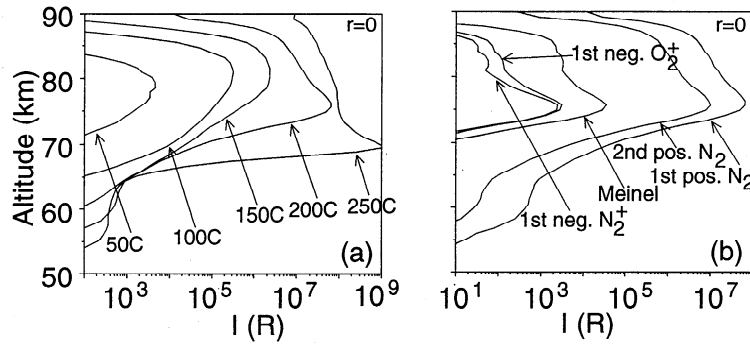


Figure 17. Instantaneous optical emission intensity. (a) Altitude scans at $r=0$ of optical emission intensity corresponding to 1st positive band of N_2 for different values of removed thundercloud charge; (b) Altitude scans at $r=0$ of optical emission intensity corresponding to different optical bands for $Q=200$ C.

the most intense (usually positive [e.g., Boccippio *et al.*, 1995]) lightning discharges.

The highly nonlinear dependence of the optical emission intensity on Q as demonstrated in Figure 16 is also supported by the altitude profiles of resultant optical emission intensity at the termination of the lightning discharge ($t = 1$ ms) as shown in Figure 17a for different values of thundercloud charges.

The altitude distribution of the optical intensities corresponding to the first and second positive bands of N_2 , Meinel and first negative bands of N_2^+ , and first negative band of O_2^+ are shown in Figure 17b. The red band (first positive band of N_2) is clearly the dominant optical emission, with its intensity being ~ 10 times larger than that of the blue (N_2 second positive band), consistent with the dominant red color of the sprites [Pasko *et al.*, 1995]. The Meinel band intensity is approximately 3 orders of magnitude below than that of the N_2 first positive band. The first negative bands of N_2^+ and O_2^+ are approximately four orders of magnitude lower than the intensity of the dominant N_2 1st positive band. These definitive predictions concerning relative excita-

tion levels of different bands provide a basis for direct comparisons with spectroscopic measurements.

3.5. Electron and Ion Conductivity

Because of the highly nonlinear nature of the interaction of quasi-electrostatic thundercloud fields with the mesosphere and the lower ionosphere it is expected that both the electron density changes and the optical emission intensities are sensitively dependent on the ambient electron and ion conductivity profiles.

Figure 18 compares the electron density changes and optical emission intensities corresponding to the three models of ambient electron number density shown in Figure 6a. All of the results shown up to this point have been for the most tenuous ambient electron density (profile 1). Two major effects associated with larger values of ambient electron density (profiles 2 and 3). First, the relative ionization changes are lower, with the maximum changes occurring at lower altitudes. Second, the corresponding optical emission intensities are dramatically reduced at the higher altitudes. Both effects are due to the shorter relaxation time of the electric field

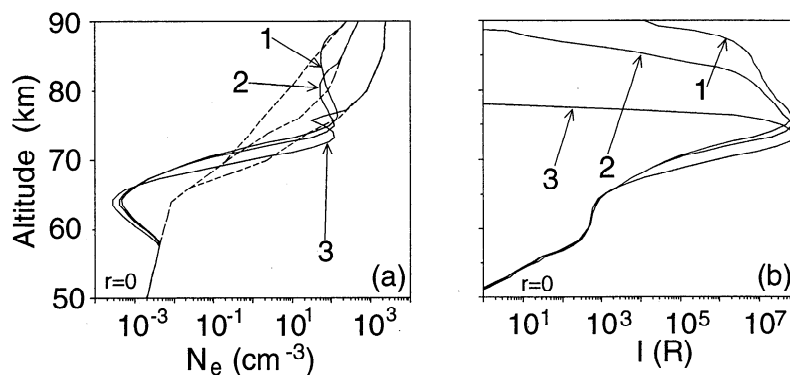


Figure 18. (a) Results of calculations for electron density changes corresponding to different models of ambient electron density (Figure 6a). The ambient profiles of electron density are shown for reference by dashed line; (b) dependence of the optical emission intensity on the model of ambient electron number density (Figure 6a). It was assumed in all cases that a charge of 200 C was removed by the lightning discharge from 10 km altitude in 1 ms. See text for explanation of profiles 1-3.

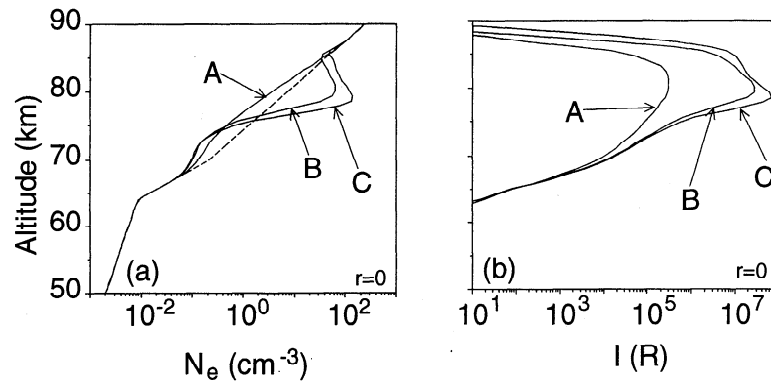


Figure 19. (right) Dependence of the optical emission intensity on ambient ion conductivity (Figure 6b). (left) Results of calculations for electron number density changes. The assumed ambient profile of electron density is shown for reference by dashed line. It was assumed in all cases that a charge of 100 C was removed by the lightning discharge from 10 km altitude in 1 ms.

at high altitudes for higher ambient electron densities. The peak intensity of optical emissions at ~ 70 km is not affected by the ambient electron number density since this quantity is defined mostly by the amplitude of the electric field (in other words by the value and amplitude of the removed thundercloud charge).

The dependence of ionization and optical effects on the ambient ion conductivity is illustrated in Figure 19. For the same value of the removed thundercloud charge (100 C), but for different ion conductivity profiles, we find either depletion in electron density due to attachment or increased density due to ionization. In terms of optical emissions, the results obtained with profiles B, C, and A differ by more than 2 orders of magnitude at ~ 80 km. We note that the ion conductivity profiles A and C are similar to ion conductivity profiles experimentally measured and/or used in previous studies [e.g., *Dejnakarintra and Park, 1974; Holzworth et al., 1985*]. Our results for these two profiles can thus be considered respectively as lower and upper bound estimates of expected levels of optical emissions and ionization changes.

3.6. Lightning Discharge Duration

The production of intense optical emissions by quasi-electrostatic fields does not necessarily require large

charge transfer rates from cloud to ground. In this context, it is important to note that in all of the results shown up to now the duration of the lightning discharge was assumed to be 1 ms. The rate of charge transfer required for achieving observable levels of optical emissions depends, in addition to the magnitude of the total removed charge, upon the conductivity profile in the 60–90 km altitude range, and the corresponding relation between the duration of the discharge and the specific relaxation time of the electric field in the conducting medium. If we assume that the value of the total removed charge remains constant the observable levels of optical emissions considered in previous sections can still be achieved with longer charge transfer times as long as they do not significantly exceed the relaxation time at 50–90 km altitudes.

To illustrate this point, we show in Figure 20 results for two different ambient ion conductivity profiles which differ by a factor of 5 at <60 km altitudes where the ion conductivity is dominant. Profile A/5 shown in Figure 20 represents conductivity values reduced by a factor of 5 with respect to profile A. We assume the electron component of the ambient conductivity to be the same for both profiles, and determined by the electron density profile 1 shown in Figure 6a.

Optical emission intensities corresponding to two dif-

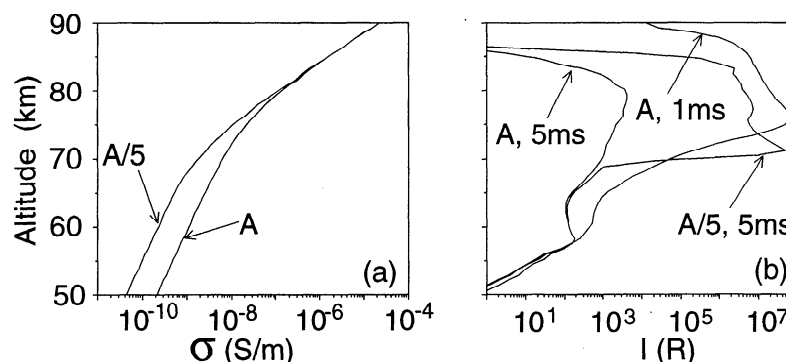


Figure 20. (right) Dependence of the optical emission intensity on (left) ambient conductivity profile and discharge duration (1 and 5 ms). It was assumed that a charge of 200 C was removed by the lightning discharge from 10 km altitude.

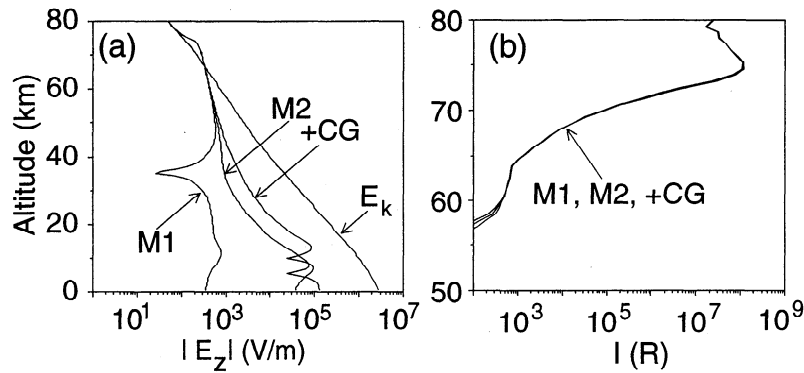


Figure 21. (right) Dependence of the optical emission intensity on the model of lightning discharge (M1, M2, +CG) (Figure 3). (left) The corresponding distribution of postdischarge electric field at $r = 0$. All calculations were performed for the removed charge value 200 C.

ferent durations of the lightning discharge (1 ms and 5-ms) for profile A, and for 5 ms duration for profile A/5 are shown in the right hand panel of Figure 20. Results shown correspond to times at the termination of the lightning discharges (i.e., 1 ms or 5 ms). The intensity of the optical emission is significantly reduced for profile A and the 5 ms discharge duration in comparison with the 1 ms case. However, the intensity distribution is similar for profile A with 1 ms discharge duration and profile A/5 with the 5 ms duration. The fast drop of the optical emission intensity above 85 km altitude for the latter case is due to the increase of conductivity of the medium resulting from ionization. Since the range of known ion conductivity profiles span more than an order of magnitude at mesospheric altitudes (Figure 6b), one can conclude that similar optical emission intensities would occur with charge removal times substantially longer than the 1 ms used in most of the calculations reported in previous sections. For lower ion conductivities, the predicted optical output would be different primarily in terms of the duration of the emission at ionospheric altitudes. The peak optical emission intensities do not depend significantly on the ambient conductivity profile since this quantity is determined primarily by the magnitude of the electric field (and thus the value and the altitude of the removed thunder-

cloud charge). The latter point was already mentioned as part of the discussion of results corresponding to different ambient electron density profiles (Figure 18), and is also illustrated by the results shown in Figure 19 indicating a saturation effect corresponding to profiles B and C. Further reduction of conductivity at mesospheric altitudes (below those represented by profile C) would not produce a significant increase in the optical emission intensity or the ionization.

Although up to now we have primarily considered the removal of ≤ 300 C of charge in ~ 1 ms, removal of larger amounts of charge (e.g., ~ 400 C) over longer times (e.g., ~ 10 ms) may lead to the formation of streamer-type channels of breakdown ionization at altitudes ~ 50 –70 km. This regime of excitation and various consequences are discussed by Pasko *et al.* [1996a].

3.7. Lightning Discharge Type

Figure 21 shows postdischarge distributions of electric field and optical emission intensity as a function of altitude for three different lightning discharge models, M1, M2, and +CG as shown in Figure 3. We note that the M2 case corresponds to the deposition of a monopole charge, in contrast to removal of charge as represented by the M1 and +CG cases.

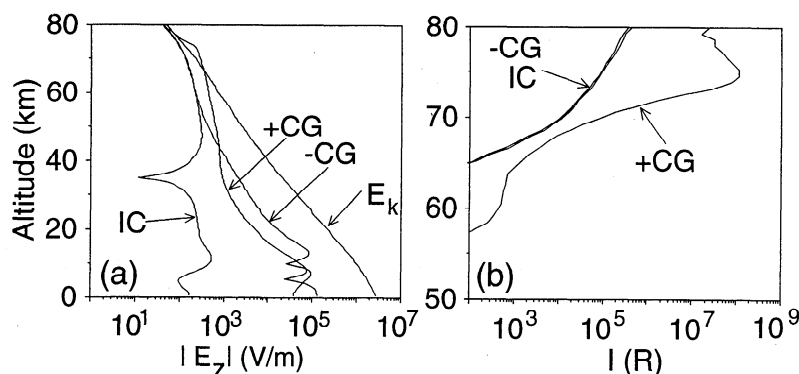


Figure 22. Results are shown in the same format as in Figure 21 but for +CG, -CG, and IC (Figure 3) models of the lightning discharge.

The results obtained for three different lightning discharge models are identical above ~ 60 km altitude, as expected since the electric field at high altitudes is defined mainly by the value of the removed/deposited charge and its altitude, independent of the charge configuration inside the cloud before or after the lightning discharge. The range of altitudes over which the electric field is independent of the lightning discharge model extends lower with increasing charge accumulation time. In this paper we use a charge accumulation time of $\tau_s = 0.5$ s [Pasko *et al.*, 1995] since optical emissions appear at altitudes well above 60 km. Calculations with τ_s longer than 0.5 s lead to identical results, and $\tau_s = 0.5$ sec value was chosen from the point of view of computational efficiency.

Figure 22 shows results for +CG, -CG and IC discharges. The +CG flashes clearly produce larger electric fields and optical emission intensities, with the optical intensity being 3 orders of magnitude above that for -CG and IC. This result is a simple consequence of the fact that +CG discharges remove charge from the higher altitude, producing larger values of postdischarge electric fields. Note that for the IC case the field of the lower removed charge significantly reduces the field of the upper charge and the resulting optical output. It should be noted that we model a +CG discharge as the removal of the thundercloud positive charge which is assumed to be located at a higher altitudes than the accompanying negative charge. In a real situation, positive charge may well be accumulated at and removed from the lower parts of the thundercloud [e.g., Boccippio *et al.*, 1995; Marshall *et al.*, 1996].

3.8. Thundercloud Charge Geometry

The dependence of optical emission characteristics on the geometry of the thundercloud charge is of particular interest since sprites usually appear above mesoscale convective systems with spatially distributed charges [Boccippio *et al.*, 1995; Marshall *et al.*, 1996; E. Williams, private communication, 1994]. Figure 23 shows the

postdischarge distribution of electric fields and optical emissions corresponding to +CG discharge for three different geometries of the thundercloud, namely, (1) Gaussian spherically symmetric charge density distributions with scale $a = 3$ km (used in most of the calculations in this paper); (2) also, Gaussian spherically symmetric distribution but with $a = 6$ km; (3) Gaussian distribution in the z direction with $a = 3$ km and flat (uniform) in the horizontal direction with a “disk” of radius 30 km.

The results in Figure 23 show that horizontally spread charges generally lead to a lower value (for the same value Q of the removed thundercloud charge) of the electric fields everywhere above the thundercloud. The size of the spherical thundercloud charges (3 and 6 km scales) does not appear to significantly affect the electric fields and optical outputs at mesospheric and ionospheric altitudes. In this connection it is interesting to note that if there were no upper conducting boundary (ionosphere), increasing the effective radius of the disk of charge would tend to approach the one-dimensional geometry of the electric field due to a sheet of charge. Since the thundercloud charge always has an image charge below the ground, the field would be enhanced between the disk and ground but would rapidly decrease above it with increasing disk radius. Since the ionospheric boundary also generates an image charge, the amplitude of the field is relatively enhanced. Results of calculations shown in Figure 23 suggest, however, that the spherical geometry gives the largest possible amplitudes of electric fields above the thundercloud. On the other hand, the disk projects a significant electric field over a wider (in the radial direction) region of space.

The electric field above the stratiform clouds associated with mesoscale convective systems have been measured by Marshall *et al.* [1996] using balloon-borne instruments. The measured amplitudes of electric fields were explained by considering the disk charge with charge density ~ 3 nC m $^{-3}$ centered at 4 km altitude, with thickness 400 m (effective surface charge density ~ 1200 nC m $^{-2}$) and diameters ranging from 20 to 200

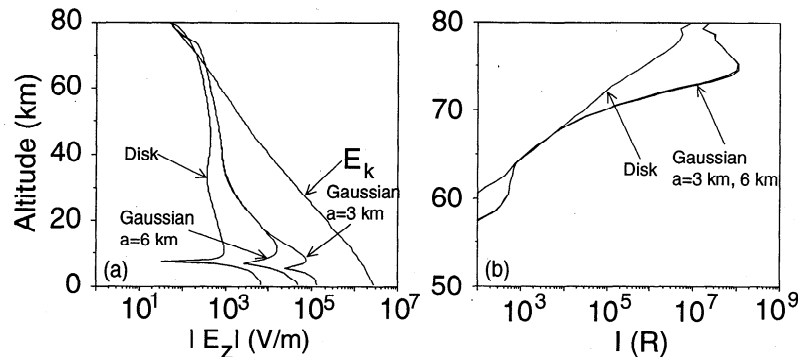


Figure 23. Results of calculations of (left) postdischarge electric fields and (right) optical emission intensities of the first positive band of N_2 for thundercloud charge distributions of (1) Gaussian spherically symmetric charge density distributions with scale $a = 3$ km (used in most of the calculations in this thesis); (2) also Gaussian spherically symmetric distribution but with $a = 6$ km; (3) Gaussian distribution in the z direction with $a = 3$ km and flat (uniform) in the horizontal direction with a “disc” of radius 30 km.

km. The authors accounted for image charge in the ground, but ignored the effects of ionospheric images. The effects of the upper ionospheric boundary must be taken into account for a correct determination of the electric field values at ionospheric altitudes and the total charge accumulated in the thundercloud, especially for horizontally spread charge distributions. We note that even relatively small values of charge (200 C) distributed over a disk with diameter 60 km (surface charge density only $\sim 100 \text{ nC/m}^2$) would lead to $\sim 1 \text{ kV/m}$ electric field change above the thundercloud (Figure 23), in excellent agreement with observations of *Marshall et al.* [1996]. Thus relatively large values $\sim 1200 \text{ nC/m}^2$ suggested by *Marshall et al.* [1996] and derived without accounting for the effects of the upper ionospheric boundary may not in fact be required for production of observed amplitudes of the electric field.

3.9. Small-Scale Structure of Sprites

It should be noted that the results of calculations presented in section 3.4 generally agree well with many of the observed features of sprites (e.g., altitude range, duration, optical emission intensity and color). The most obvious discrepancy between the model results shown in Figure 16 and the video observations is that due to the geometry of the postdischarge electric fields at mesospheric altitudes the volume of the predicted optical emission has a tendency to expand in the horizontal direction rather than to form the thin vertical structure typically observed in sprite phenomena. In this regard we note that the lateral dimension of the optical emissions shown in Figure 16b, 16c and 16d agrees with the overall horizontal extent of clusters of sprites and would agree very well with observations if there is an additional mechanism which leads to spatial stratification of the emission.

The vertically striated structure of sprites can be due to the development of streamer type ionization channels of breakdown ionization which may be produced by discharges removing large amounts of charge which are usually accompanied by long (several milliseconds)

continuing currents [*Pasko et al.*, 1996a]. In this case clusters of sprites can result from local inhomogeneities of mesospheric conductivity of any origin (e.g., electron precipitation from magnetosphere, meteors, ionization left from previous sprite, etc) [*Pasko et al.*, 1996a].

Another simple mechanism which could lead to spatial stratification of the emission is connected with spatial modulation of the neutral density in the mesosphere above thunderstorms. As can be seen from Figures 8 and 9, the effective coefficients of ionization ν_i and attachment ν_a and optical excitation of neutrals ν_k are very sensitive to the value of neutral density N and can change several orders of magnitude in response to only 20–30 % variation in N . To illustrate this point we introduce in our model a region with a depletion in ambient neutral density as shown in Figure 24. The region is centered at 75 km altitude and has a Gaussian distribution similar to that introduced for thundercloud charge density in section 2.2 but with scale 10 km in vertical and 7 km in horizontal direction. The maximum perturbation of the neutral density is assumed to be 30 %. In Figure 25 we compare results of model calculations for $Q=150\text{C}$ with and without the depletion in the ambient neutral density. In the two bottom panels of Figure 25 one can see the formation of an ionization/luminous column with spatial structure significantly different from that shown in the two top images for the case with no perturbation in N . We note also a significant enhancement (factor of ~ 5) in the maximum optical emission intensity.

The braking of gravity waves at mesospheric altitudes into small-scale structures [e.g., *Walterscheid and Schubert*, 1989] and the resultant of order $\sim 20\%$ modulation of the atmospheric neutral density [*Walterscheid and Schubert*, 1989] may be an essential accompaniment of sprite phenomena. Upward propagating gravity waves may be generated by intensive tropospheric convection associated with mesoscale convective systems [e.g., *Fovell et al.*, 1992]. There is experimental evidence that these waves may play a role as a heater of the neutral atmosphere at mesospheric altitudes [e.g., *Taylor*, 1979]. This kind of heating may lead to overall depletion in the neutral density at mesospheric altitudes and result in lowering of the electric field thresholds of ionization and excitation of neutrals (see Figures 8 and 9). Mechanisms associated with upward propagating gravity waves launched by intense convection in mesoscale convective systems may explain why sprites usually occur several hours after the beginning of the storm, which is roughly the time of travel of a gravity wave from the troposphere to mesospheric altitudes, assuming the typical vertical group velocity of these waves to be on the order of several meters per second [e.g., *Taylor*, 1979].

The heating of the neutral atmosphere by static thundercloud electric fields through collisional transfer of energy from heated electrons to neutrals on a timescale of several hours (*V. P. Pasko et al.*, submitted manuscript, 1996) may also contribute to changes in mesospheric neutral density above thunderstorms which produce sprites.

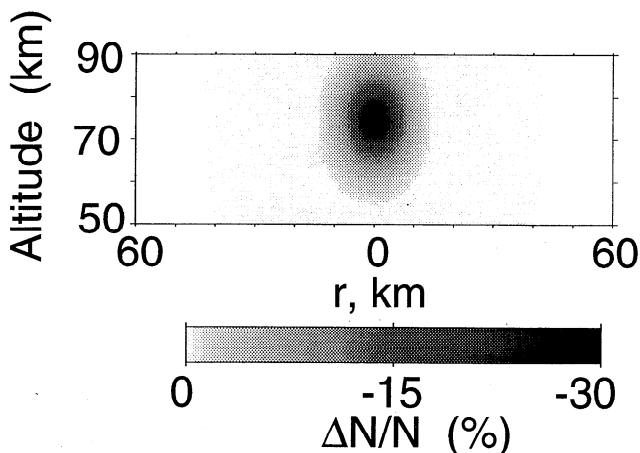


Figure 24. A hypothetical depletion of the neutral density at mesospheric altitudes used to obtain results shown in Figure 25.

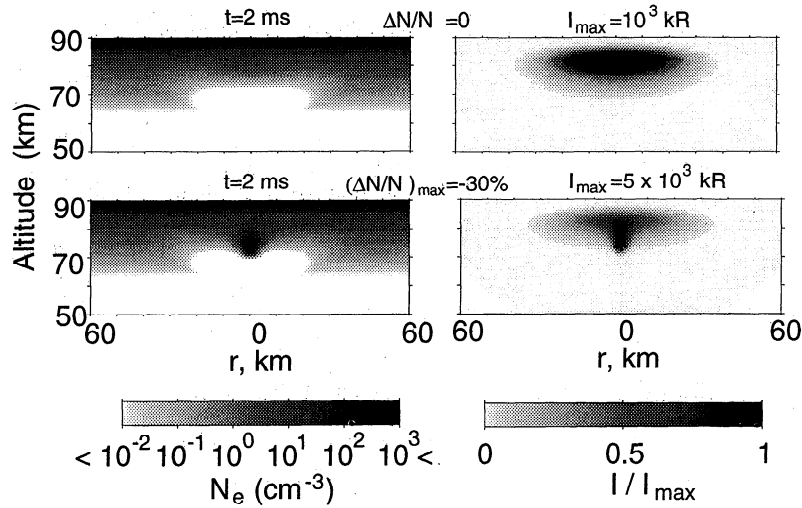


Figure 25. Comparison of the model results with and without perturbation in ambient neutral density shown in Figure 24. (left) The altitude distribution of the electron density N_e and for thundercloud charge $Q=150$ C at the moment of time $t=2$ ms. (right) The corresponding distribution of the time-averaged intensity (in units of Rayleighs) of emissions of the 1st positive band of N_2 .

3.10. Relaxation Times of Quasi-Electrostatic Fields

The dynamics of the electric field in the conducting medium above thunderclouds directly control the ionization changes and the duration of optical emissions associated with sprites. An important aspect of our model with respect to previous work on the relaxation of quasi-electrostatic fields [Dejnakarintra and Park, 1974; Greifinger and Greifinger, 1976; Hale and Baginski, 1987; Baginski et al., 1988; Hale, 1994] is the self-consistent modeling of the conductivity σ , as discussed in section 2.5. To demonstrate the importance of the self-consistent treatment of conductivity in comparison with previous work, we compare in Figure 26 the temporal variation of the electric field $|E_z|$ at 70 and 80 km for three different treatments of conductivity

ity σ for the case of removal of a monopole charge (case M1 shown in Figure 3).

At $z=80$ km, the electric field $|E_z|$ for case a is ~ 4 times that for case b, and initially exhibits ~ 3 times longer time duration, followed by a faster decrease, resulting from the initial decrease of conductivity σ due to heating followed by its increase due to ionization at later times. For case d at both altitudes (70 and 80 km) the relaxation rate of the electric field slows down even in comparison with cases a and b; this effect is due to the formation of the quiescent electric field around the source charge. This steady field can be found as the stationary solution of the problem of a point charge in a medium with exponentially increasing (in altitude) conductivity [e.g., Holzer and Saxon, 1952]. In all cases, we see significant slowing down of the relaxation rate of the electric field in comparison with the local ambient

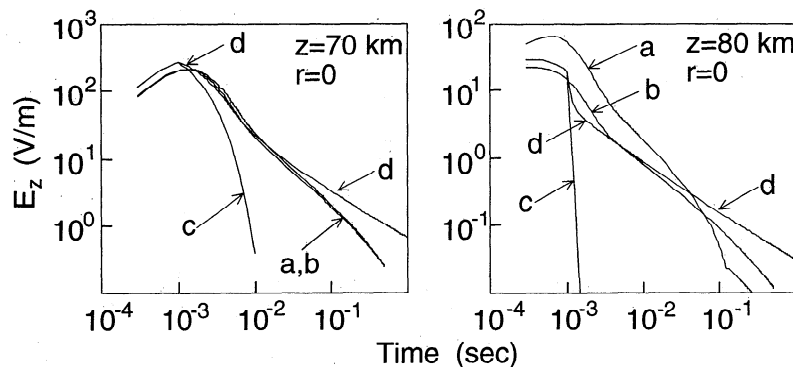


Figure 26. The vertical component of the electric field at two selected altitudes at $r = 0$ as a function of time since the beginning of the lightning stroke for a 200 C source charge for different solutions of conductivity σ : a, self-consistent formulation; b, conductivity kept constant in time; c, relaxation with the local ambient relaxation time (ϵ_0/σ); d, same as curve b but for charge deposited during 1 ms (M2, Figure 3) (rather than removal) at the beginning of the simulation.

ϵ_0/σ (marked c in Figure 26) rate. The most recent discussion of this effect, which has been observed experimentally and extensively studied theoretically, is given by Hale [1994, and references therein].

Since the slowing down of the electric field relaxation rate is observed on a millisecond time scale [e.g., Dejenakarintra and Park, 1974; Baginski et al., 1988; Hale, 1994] our quasi-electrostatic formulation which is valid for the near zone fields is fully sufficient for the investigation of the temporal evolution of the quasi-static fields and its consequences in the form of heating, ionization and optical emissions. That this is so can also be confirmed by recent results of Baginski and Hodel [1994] who provide a detailed comparison of the solution of the system of (1) and (2) with the full system of Maxwell equations.

The slowing down effect can be physically understood as follows. The atmospheric conductivity exponentially increases with altitude. There exists an altitude below which we can consider charges (both thundercloud and induced polarization charges in the conducting atmosphere) to be "stationary" on a certain timescale. The slowing down of the electric field relaxation can be interpreted as the establishment of a quasi-stationary solution above this "stationary" charge. As time progresses, the imaginary boundary below which we can consider charges and associated fields to be stationary moves downward [e.g., Greifinger and Greifinger, 1976]; however, the rate of the field and charge relaxation above this boundary always remains slower than the local relaxation rate ϵ_0/σ . At each altitude above this boundary there is a nonvanishing value of induced charge and current density which is a consequence of the inhomogeneity of the atmospheric conductivity [Greifinger and Greifinger, 1976]. The relaxation rate would be even further slowed down if there is a source charge which is maintained by an external effect (e.g., regeneration of charge within the thundercloud due to updraft). Such a circumstance is represented by the deposition of charge over 1 ms, as in the case marked d in Figure 26.

The imaginary downward moving boundary mentioned above is essentially the "moving capacitor plate" model introduced first by Greifinger and Greifinger [1976] and successfully used by Hale and Baginski [1987] to estimate the current which flows to the ionosphere following a lightning stroke. Greifinger and Greifinger [1976] define this boundary as separating two regions dominated by conduction (above) and displacement (below) currents.

Any persisting charges at low altitudes constitute a source of electric field at high altitudes, so that the electric field at high altitudes completely relaxes to zero only when the last remaining charges dissipate at low altitudes, a process which occurs with long relaxation times due to low atmospheric conductivity. Until such time that the polarization charges at the lowest altitudes dissipate away, the electric fields at high altitudes continuously goes through a series of quasi-stationary states corresponding to persisting at low altitudes charges. This effect leads to the apparent slowing down of the relaxation of the electric fields.

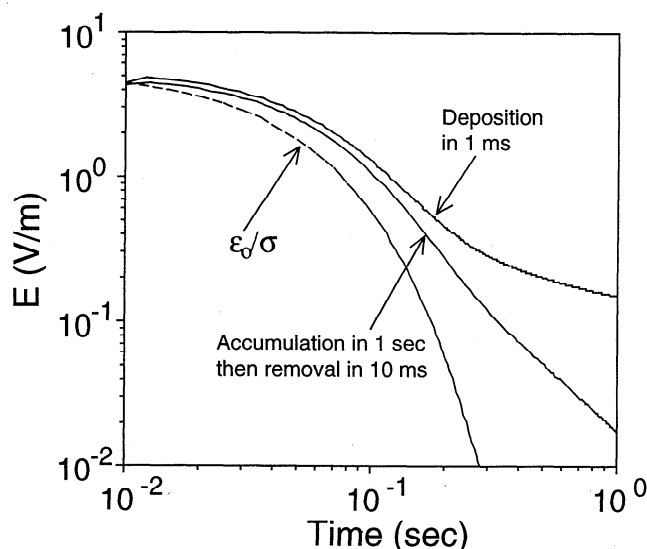


Figure 27. One-dimensional relaxation of the electric field. The electric field at altitude 50 km as a function of time: (1) relaxation with the local ambient relaxation time (ϵ_0/σ); (2) deposition in 10 ms of a disk of charge of 10 C with diameter 300 km and vertical extent 3 km at altitude 20 km; (3) the same as point 2 but the charge was accumulated during 1 s and then removed in 10 ms.

An important role is played by surface charges induced at the highly conducting ground and lower ionospheric boundaries which are assumed to be maintained at a constant potential. These charges change dynamically in time consistent with the electric fields and correspondingly affect the dynamics of the fields (see further discussion in Appendix B). The slowing down effect is not a property of two-dimensional system and is also observed in one dimensional geometry.

To illustrate the above points, we show in Figure 27 results obtained for cases similar to those shown in Figure 26b,d, but for the deposition and removal of a "disk" of charge of 10 C with radius 150 km and vertical extent 3 km. The radial size of the system was assumed to be also 150 km by adopting the boundary condition $\partial\varphi/\partial r = 0$ at $r = 150$ km. The electric field in this case is essentially one-dimensional and is directed vertically everywhere in the system. Similar to those of Figure 26, results of Figure 27 show slowing down of the electric field relaxation. Note that the field shown is that at 50 km altitude so that the relaxation of the field in this case is entirely determined by the gradients of conductivity and persisting charges (no heating effects included).

Another one-dimensional problem providing clear physical illustration of the effect, which also has a simple analytical solution using the "moving capacitor plate" model of [Greifinger and Greifinger, 1976], is given in Appendix B.

In summary, we can identify three separate physical effects which contribute to the slowing down of the relaxation rate of the quasi-static electric field: (1) the decrease of the ambient electron component of

the conductivity due to selfconsistent heating by quasi-electrostatic fields; (2) the generation of additional surface charges at the highly conducting ground and the lower ionospheric boundaries; (3) the establishment of quasi-stationary distributions of the electric fields and charge densities around persisting thundercloud charges and polarization charges in the conducting atmosphere above the thundercloud.

3.11. Comparison With Auroral Optical Emissions

It is interesting to compare the spectral content of optical emissions associated with aurorae and those produced at the same altitudes by electrons heated by electric fields resulting from intensive cloud to ground lightning discharges.

The typical omnidirectional flux of auroral electrons (in electrons $\text{cm}^{-2} \text{s}^{-1} \text{eV}^{-1}$) can be approximated by the expression [Meier *et al.*, 1989]:

$$\Phi(\mathcal{E}) = \Phi_M(\mathcal{E}) + 0.4\Phi_{\max} \frac{\mathcal{E}'}{\mathcal{E}} e^{-\frac{\mathcal{E}'}{b}}, \quad (13)$$

where

$$\Phi_M(\mathcal{E}) = \frac{P\mathcal{E}}{2\pi(\mathcal{E}')^3} e^{-\frac{\mathcal{E}}{\mathcal{E}'}} \quad (14)$$

and Φ_{\max} is the maximum value of Φ_M , \mathcal{E} is energy in keV, and $b = 0.8\mathcal{E}'$ if $\mathcal{E}' < 0.5$ keV, or $b = 0.1\mathcal{E}' + 0.35$ if $\mathcal{E}' \geq 0.5$ keV, \mathcal{E} is the characteristic energy, and P is the energy flux. The excitation rate of the k th excitation process involving the j th species can be calculated as

$$\nu_k = N_j \int_{\mathcal{E}} \Phi(\mathcal{E}) \sigma_k(\mathcal{E}) d\mathcal{E}, \quad (15)$$

where σ_k corresponds to k th excitation process cross section.

Results of calculations of ν_k using (15) for selected optical bands and range of the characteristic energies \mathcal{E}' 0.1–10 keV for $P = 30 \text{ ergs cm}^{-2} \text{s}^{-1}$ are shown in Figure 28b along with the electron flux for three selected values of \mathcal{E}' (Figure 28a). The 1st negative and Meinel bands of N_2^+ are clearly dominant, and the auroral emissions

exhibit a rich spectral complexity in comparison with those produced by quasi-electrostatic fields (e.g., Figure 17b).

Figure 28b shows the excitation rates rather than the emission rates. At altitudes of ~ 85 km used for our calculations, the Meinel N_2^+ band is quenched, since the quenching height for this band is ~ 90 km. The resulting emission rate is thus ~ 2 –3 times lower than the excitation rate plotted in Figure 28b. The rest of the bands shown have quenching heights much lower than 85 km so that the corresponding excitation rates can be interpreted as emission rates.

The primary reason for the spectral differences between in the auroral precipitation and quasi-electrostatic heating cases is the relative structure of the electron distribution function as a function of energy and the corresponding excitation cross sections. In the case of electron heating by quasi-static electric fields, the distribution function sharply decreases with increasing energy in the region of electron energies of 10–15 eV (due to the effective loss of electron energy as a result of inelastic collisions [Taratenko, 1993]) as illustrated in Figure 28c, for $h = 85$ km and an applied electric field of 45 V/m. For illustration, the distribution of excitation cross sections for N_2 1st positive and N_2^+ Meinel bands [Taratenko, 1993] are also shown in Figure 28c. In the auroral case, the distribution function has a wide extent and covers a broad energy range up to 10^4 – 10^5 eV (Figure 28a). In simpler terms, the secondary electron distribution in aurorae are produced by impact of higher energy precipitating electrons and thus has a distribution with larger numbers of electrons at higher energies.

4. Summary

A new form of electrodynamic coupling between thunderstorms and the mesosphere and lower ionosphere has been identified, involving heating, ionization, and optical emission effects produced by quasi-electrostatic thundercloud fields, and accounting for the basic features of mesospheric optical emissions called sprites.

Sprites are proposed to be a consequence of large electric field transients capable of causing electron heating,

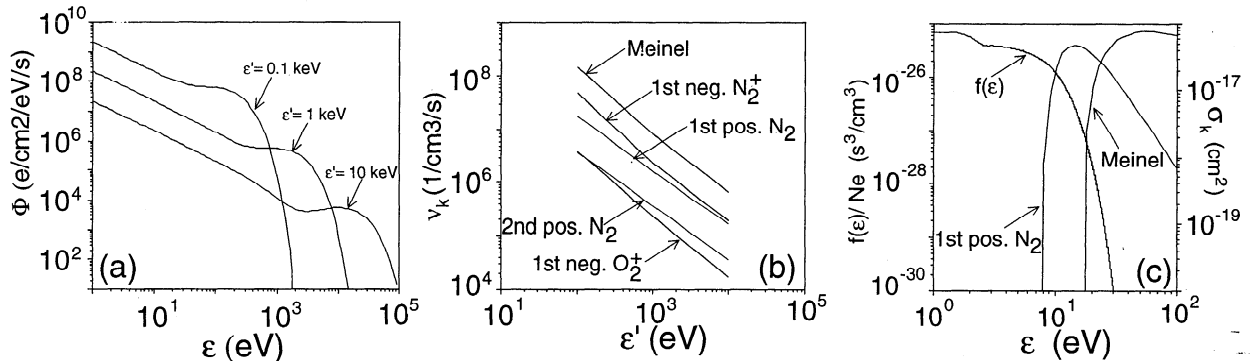


Figure 28. (a) Omnidirectional flux of auroral electrons; (b) excitation rates of selected optical bands corresponding to Figure 28a; (c) typical distribution function of heated electrons and cross sections of the optical excitation of 1st positive band of N_2 and Meinel band of N_2^+ .

breakdown ionization and excitation of optical emissions at mesospheric altitudes following the removal of a thundercloud charge by a cloud-to-ground discharge. These transients can be produced by the combined action of induced spatially distributed space charge which exists in the region between the thundercloud tops and the lower ionosphere and the charge left in the cloud after the lightning discharge. Results obtained with a two dimensional and selfconsistent model of the nonlinear upward coupling of quasi-electrostatic thundercloud fields are consistent with the observed spectra, temporal duration, and spatial extent of sprites.

The heating of the mesosphere/lower ionosphere by quasi-electrostatic fields can lead to significant modification of the conductivity of these regions. Model calculations predict significant (several orders of magnitude) modification of the lower ionospheric conductivity in a region with 50-60 km transverse extent. This modification can be in the form of depletions of electron density due to dissociative attachment to O_2 molecules or enhancements of electron density due to breakdown ionization of O_2 and N_2 . Ionization changes produced by consecutive lightning discharges can accumulate, leading to the build up of ionization "bubbles" or attachment "holes" above thunderstorms.

Results of the model calculations corresponding to fast (~ 1 ms) removal of 100-300 C of thundercloud charge from 10 km altitudes are in good agreement with observations of the upper part ("head" and "hair" [Sentman *et al.*, 1995]) of the sprites. The typical region of brightest optical emission has horizontal and vertical dimensions ~ 10 km, centered at altitudes ~ 70 km and is interpreted as the head of sprite. Our model results also indicate the formation of low intensity glow ("hair") above this region due to the excitation of optical emissions at altitudes ~ 85 km during the ~ 500 μ s at the beginning of the lightning discharge. Comparisons of the optical emission intensity of the 1st and 2nd positive bands of N_2 , Meinel and 1st negative bands of N_2^+ , and 1st negative band of O_2^+ show that the 1st positive band of N_2 is the dominant emission under conditions of heating by quasi-electrostatic thundercloud fields.

The dependence of quasi-electrostatic heating upon the altitude profile of ion conductivity, number density of electrons and duration of the lightning discharge indicates that the level of optical emissions is defined mainly by the relation between the lightning discharge duration and the conductivity of the upper atmosphere (i.e., relaxation time of the electric field in the conducting medium). For low ambient conductivities the lightning discharge duration can be significantly longer than 1 ms and still produce similar levels of optical emissions. The maximum possible intensity of optical emissions is determined mainly by the value of the removed thundercloud charge and its altitude.

Comparison of the model results for different types of lightning discharges (+CG, -CG, IC) indicate that positive cloud-to-ground discharges lead to the largest electric fields and optical emissions at ionospheric altitudes but only because they are typically associated with the

removal of larger amounts of charge from higher altitudes. Studies of different geometries of thundercloud charges suggest that spherically distributed charges produce more intense electric fields and optical emissions than horizontally spread charges of the same magnitude.

The preexisting inhomogeneities in the mesospheric conductivity and the neutral density may contribute to the formation of the vertically striated fine structure of sprites and explain why sprites often repeatedly occur in the same place on the sky as well as their clustering. The heating of the neutral atmosphere at mesospheric altitudes above mesoscale convective systems is suggested as a possible necessary condition for the appearance of sprites.

The slowing down of the relaxation rate of the electric fields in the atmosphere/lower ionosphere following lightning discharges can be explained in terms of combined action of the following physical effects: (1) the decrease of the ambient electron component of the conductivity due to selfconsistent heating by quasi-electrostatic fields; (2) the generation of additional surface charges at the highly conducting ground and the lower ionospheric boundaries; (3) the establishment of quasi-stationary distributions of the electric field and charge density around persisting thundercloud charges and polarization charges in the conducting atmosphere above the thundercloud.

Appendix A: Comparison With Kinetic Solutions and Swarm Experiments

In this appendix, we evaluate the validity of parametric approximations for mobility, ionization, attachment and optical excitation rates (sections 2.5.1, 2.5.2, 2.5.3, and 2.6) with the results of kinetic solutions [Taranenko *et al.*, 1993a, b] and with the results of the electron swarm experiments where available [e.g., Davies, 1983]. For this purpose, we consider the altitude profile (at $r = 0$) of the electric field which approximately corresponds to a charge of 300 C placed at 10 km altitude km (M2 model from Figure 3). We then divide the altitude range from 10 to 90 km in equidistant intervals with 1-km steps. At each altitude, the value of the electric field is divided into 50 linear intervals so that the first value is 0 and last value is the maximum value of the electric field at this altitude. The resulting discretization of the electric fields and altitudes is illustrated in Figure 29. The stationary electron distribution function $f(v)$ corresponding to the each of the points shown in Figure 29 (i.e., for different electric fields and densities of atmospheric gas) is obtained from the solution of the Boltzman equation, taking into account inelastic collisions consisting of rotational, vibrational, optical, dissociative, dissociative with attachment, and ionizational losses [Taranenko *et al.*, 1993a]. The mobility, ionization, attachment, and optical excitation rates are calculated using the obtained distribution functions and known cross sections for these processes [Taranenko *et al.*, 1993a, b]. Results obtained with this approach are

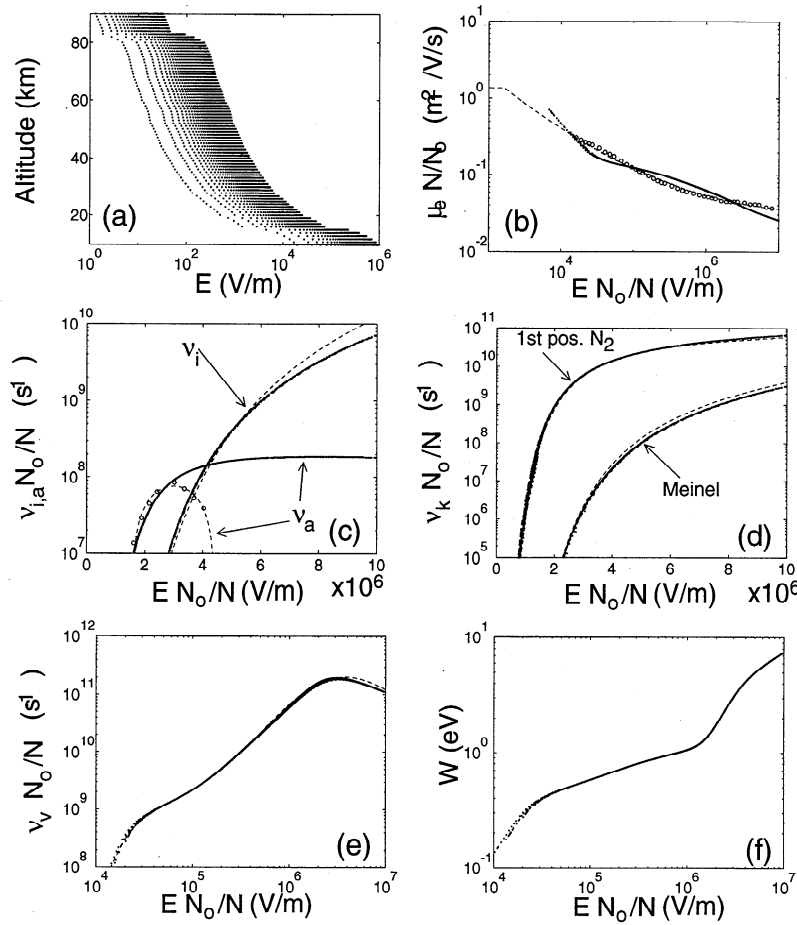


Figure 29. Comparison of analytical approximations with kinetic solutions and results of swarm experiments. (a) The discretization of altitudes and electric field values for the kinetic solutions; (b) the electron mobility corresponding to different models is shown in the same format as in Figure 7; (c) the ionization and attachment coefficients corresponding to different models are shown in the same format as in Figure 8; (d) the excitation coefficients of selected optical bands corresponding to different models are shown in the same format as in Figure 9; (e) the excitation coefficient of vibrationally excited N_2 molecules; (f) the average energy of the electron distribution.

directly comparable to swarm laboratory experiments [e.g., Davies, 1983] in which when the electron mobility is measured for different magnitudes of applied electric fields and ambient neutral gas densities.

A1. Electron Mobility

The electron mobility can be calculated as

$$\mu_e = \frac{1}{EN_e} \int v f(v) d^3v \quad (A1)$$

where the distribution function is assumed to be normalized so that $N_e = \int f(v) d^3v$. Results are shown in Figure 29b by dots. We also show the corresponding values obtained from experimental measurements by Davies [1983] (open circles) and those obtained using the analytical approximation (5) (dashed line). For lower values of the electric fields ($EN_0/N < 10^4$ V/m) the analytic approximation (5) is supported by measurements of Hegerberg and Reid [1980] (not shown).

The normalized mobility values of $\mu_e N/N_0 = 1.36$ m²V⁻¹s⁻¹ for $EN_0/N < 1.62 \times 10^3$ V m⁻¹ correspond to the thermal state of the electrons (with no heating). The value of the mobility in this region of electric fields is found to be in good agreement with that derived from hydrodynamic equations using effective collision frequencies and average fractions of energy transferred in one collision from electrons to neutrals at an electron temperature $T_e = 200$ K [Gurevich, 1978, pp. 32, 99, 103]. The results of the three different approaches (kinetic, experimental, analytical) shown in Figure 29b agree with each other reasonably well.

A2. Ionization and Attachment Coefficients

The ionization ν_i and attachment ν_a coefficients can be calculated as

$$\nu_i = \frac{N}{N_e} \int v f(v) \sigma_i(v) d^3v, \quad (A2)$$

$$\nu_a = \frac{N_{O_2}}{N_e} \int v f(v) \sigma_a(v) d^3v, \quad (A3)$$

where σ_i and σ_a are corresponding cross sections. Comparison of the results of kinetic calculations (A2) and (A3) (dots), and the analytical approximations (6) and (7) (dashed lines) for ν_i and ν_a are shown in the Figure 29c. For the attachment coefficient we also show results of experimental measurements by Davies [1983] (open circles). We note once again the reasonable agreement between the different approaches. For the electron attachment coefficient in the range of electric fields $EN_o/N > 4 \times 10^6 \text{ V m}^{-1}$ we see a significant difference between the experimental data and the results of kinetic solutions (most probably caused by detachment effects as discussed by Davies [1983]); however, in this region of electric fields the attachment coefficient becomes much smaller than the ionization coefficient so that the relative inaccuracy of the parametric model does not affect our numerical results.

A3. Optical Emissions

The excitation rate per one electron of a given energy state k for a particular species j has the value

$$\nu_k = \frac{N_j}{N_e} \int v f(v) \sigma_k(v) d^3v, \quad (A4)$$

where σ_k is the cross section for excitation of state k . For the sake of brevity in Figure 29d we show only results corresponding to the excitation rates of the 1st positive band of N_2 and the Meinel band of N_2^+ . The comparison between kinetic solutions (A4) (dots) and the analytical approximations (10) (dashed lines) demonstrate that the later can be used with negligible error, as we have done in our model calculations.

A4. Vibrational Excitation of Molecular Nitrogen

In Figure 29e we show the excitation rate (per one electron) of the vibrationally excited N_2 molecules:

$$\nu_v = \frac{N_2}{N_e} \int v f(v) \sigma_v(v) d^3v, \quad (A5)$$

where σ_v is the cross section corresponding to this process [Taranenko, 1993]. Although not discussed in this paper, production of vibrationally excited N_2 molecules may play an important role in the chain of reactions leading to 4.3- μm infrared emissions of CO_2 [e.g., Picard *et al.*, 1987]. Results of kinetic solutions in this case can also be approximated by a relatively simple analytical formula:

$$\log(\nu_v \frac{N_o}{N}) = \sum_{i=0}^5 a_i x^i \quad (A6)$$

where $x = \log(EN_o/N)$, and $a_0 = -1284.6, a_1 = 1154.1, a_2 = -408.37, a_3 = 71.513, a_4 = -6.1882, a_5 = 0.21158$, which is shown in Figure 29e by a dashed line.

The approximation given by (A.5) is valid for the range of electric fields $10^4 < EN_o/N < 10^7 \text{ V m}^{-1}$.

A5. Average Electron Energy

For illustrative purposes in Figure 29f we provide the average energy of the electron distribution

$$W = \frac{1}{N_e} \int \frac{m_e v^2}{2} f(v) d^3v \quad (A7)$$

as a function of the electric field. Calculations show that even in cases of relatively strong ionization, as shown in Figure 12 for the removed charge 250 C, the peak average energy of the electron distribution does not exceed $\sim 5 \text{ eV}$, indicating that most of the ionization is produced by the relatively small number of electrons in the tail of the electron distribution function which appear in the region of energies of $\sim 15 \text{ eV}$ (corresponding to ionization threshold of N_2 and O_2).

Appendix B: One-Dimensional Relaxation of Quasi-Electrostatic Fields

To better appreciate the physics of the relaxation of the electric field in a medium with conductivity gradients consider the following one-dimensional problems.

The one-dimensional equation describing the dynamics of the electric field can be derived from the continuity equation (3) in the form:

$$\frac{\partial E_z}{\partial t} + \frac{\sigma}{\epsilon_o} E_z = f(t) \quad (B1)$$

where $f(t)$ is a function which does not depend on z . It is important to note that if the value of the electric field is maintained (due to some external source current) at the constant value E_o at a certain boundary, for example, at $z = 0$, then $f(t)$ is forced to be constant and does not depend on time.

If the electric field at $t = 0$ is introduced in the system as a "deposition" of an equivalent amount of surface charge $\rho_o = \epsilon_o E_o$ at $z = 0$, then this field will relax in time to a stationary solution of (B1)

$$E_z = E_o \frac{\sigma_o}{\sigma(z)} \quad (B2)$$

with local relaxation rate $\epsilon_o/\sigma(z)$ at each altitude as

$$E_z = E_o \left[\left(1 - \frac{\sigma_o}{\sigma}\right) e^{-\frac{\sigma}{\epsilon_o} t} + \frac{\sigma_o}{\sigma} \right] \quad (B3)$$

If now we deposite to the surface $z=0$ a charge of opposite sign $\rho_s = -\epsilon_o E_o$, which effectively reproduces in one dimension the charge removal studied in two-dimensional case earlier in this paper, then the electric field at each altitude again will relax with the local relaxation rate as

$$E_z = E_o \left(\frac{\sigma_o}{\sigma} - 1 \right) e^{-\frac{\sigma}{\epsilon_o} t} \quad (B4)$$

so that $f(t)=0$.

An important result which follows from this simple illustration is that the function $f(t)$ is always defined on the boundaries of the system by external (forced) sources. Any deviation of the relaxation rate of the electric field from the local ambient is defined mostly by this function $f(t)$, for example, by dynamics of external sources.

To avoid any confusion in connection with previous discussion in section 3.9, we note that the establishment of stationary solutions of type (B2) can be perceived by an observer as a slowing down of the electric field relaxation rate in comparison with the local ambient one. If $f(t)$ is constant in (B1) then the electric field will approach the stationary solution (B2) with the local relaxation rate at each altitude z in accordance with (B3).

Further, we note that in real situations the Earth's surface and the ionosphere are maintained under constant potentials, so that $f(t) \neq 0$ (in other words the boundary values of the electric field and corresponding charge densities are functions of time) which naturally leads to deviations of the electric field relaxation from the local ambient rate as illustrated in previous results of our simulations.

Now consider the time dynamics of the establishment of the fair weather electric field between two surfaces with constant potentials. We assume that there is initially no space charge in the system and at $t = 0$ introduce a potential $V_o = 3 \times 10^5 \text{ V m}^{-1}$ at $z=0$ and $V = 0$ at $z = D = 60 \text{ km}$ horizontal surfaces. Assuming the conductivity to be $\sigma(z) = \sigma_o e^{z/h}$ with σ_o and h corresponding to case A shown in Figure 6b, the stationary solution for the electric field is simply:

$$E(z) = \frac{\sigma_o \rho_s}{\sigma(z) \varepsilon_o} \quad (\text{B5})$$

where ρ_s is a surface charge induced on the surface of Earth.

Figure 30a shows by dashed lines the results of a numerical solution of this problem for the altitude distribution of the electric field at different instants of time. One can see growth of the electric field near the ground (associated with growth of the surface charge ρ_s) and relaxation of the field at high altitudes. As time progresses the electric field approaches a stationary ("fair weather") exponential distribution similar to (B5). We note that in this one dimensional case the relaxation of the electric field also demonstrates a significant deviation from relaxation with the local ambient rate (Figure 30b).

It can be shown that the exact analytical solution of this problem can be expressed in the form of an integral equation for the potential similar to that derived by Illingworth [1972] in a two-dimensional case; the solution of which, however, requires numerical efforts comparable with the finite difference solution of the original problem. A significant simplification can be achieved by using the "moving capacitor plate" model of Greifinger and Greifinger [1976]. This model defines two regions (1 and 2 as shown in Figure 31) separated by a boundary h_i . The boundary moves downward from the high-altitude ionosphere with time t after introduction of the potential difference V_o (which is qualitatively similar to the injection of a Wilson monopole corresponding to a lightning stroke [Hale and Baginski, 1987, and references therein] in a two-dimensional case) giving a time-dependent "ionospheric height":

$$h_i = h \ln \left(\frac{\varepsilon_o}{\sigma_o t} \right), \quad (\text{B6})$$

In the region 1 the displacement current is dominant, and the electric field can be calculated as in a free space:

$$E_1(t) = \frac{V_o - V'(t)}{h_i(t)} \quad (\text{B7})$$

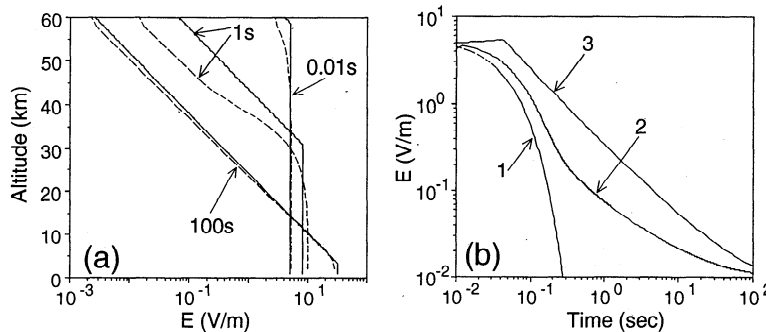


Figure 30. Comparison of numerical and analytical solutions for the relaxation of the electric field. The electric field as a function of time corresponding to sudden introduction at $t = 0$ of potential difference $V_o = 3 \times 10^5 \text{ V/m}$ between Earth surface ($z = 0$) and altitude $z = 60 \text{ km}$. (a) Dashed line corresponds altitude distribution of the electric field at three instants of time obtained from numerical simulations. Solid line corresponds to analytical solutions (B7), (B8), and (B10) using the moving capacitor plane model. (b) Dynamics of the electric field at altitude 50 km : 1, relaxation with the local ambient relaxation time (ε_o/σ); 2, result of the numerical simulation (corresponds to dashed lines shown in Figure 30a); 3, result of the analytical solutions (B7), (B8), and (B10) (corresponds to solid lines shown in Figure 30a).

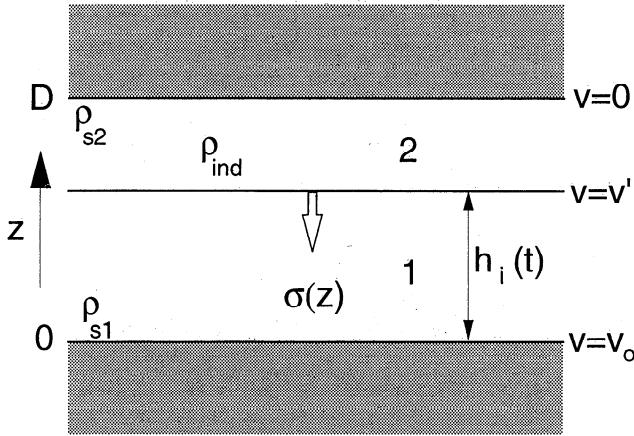


Figure 31. Moving capacitor plate model.

where V' is the value of the potential at the h_i surface, which is generally a function of time to be found.

In the region 2 the conduction current is dominant, and the electric field can be expressed as a "stationary" solution of type (B5), assuming continuity of the field at the boundary h_i as:

$$E_2(z, t) = \frac{\sigma(h_i)}{\sigma(z)} E_1(t) \quad (B8)$$

Having integrated $-\partial V_2/\partial z = E_2(z, t)$ subject to the boundary condition $V_2(D) = 0$, the solution for the potential in region 2 can be expressed as

$$V_2 = hE_1 \left[\frac{\sigma(h_i)}{\sigma(z)} - \frac{\sigma(h_i)}{\sigma(D)} \right] \quad (B9)$$

Equations (7) and (9) at $z = h_i$ are combined to yield

$$V' = \frac{V_o \frac{h}{h_i} \left[1 - \frac{\sigma(h_i)}{\sigma(D)} \right]}{1 + \frac{h}{h_i} \left[1 - \frac{\sigma(h_i)}{\sigma(D)} \right]} \quad (B10)$$

which completely defines dynamics of the electric field in space and time as given by (B7) and (B8).

The comparison of the approximate solution obtained with the results of numerical simulations is shown in Figure 30 and demonstrates the general agreement between the two solutions in terms of the altitude structure of the electric field as a function of time (Figure 30a) as well as in terms of the slowing down of the field relaxation at the selected altitude 50 km (Figure 30b). The differences between the two solutions as observed in Figure 30 are due to the apparent roughness of the moving capacitor plate model which treats the transition between the displacement current and conduction current regions (1 and 2 as shown in Figure 31) as a sharp boundary.

It is illustrative to consider different limiting cases of the approximate analytical solutions (B7), (B8), and (B10).

At time $t = 0$, $h_i \rightarrow D$ and $V' = 0$. For this case we simply have $E_1 = V_o/D$ and $E_2 = E_1$.

At time $t \rightarrow \varepsilon_o/\sigma_o$, $h_i \rightarrow 0$ and $V' = V_o$. The electric field in region 1 can be found as

$$E_1 = -\lim_{h_i \rightarrow 0} \frac{dV'}{dh_i} = \frac{V_o}{h \left(1 - \frac{\sigma_o}{\sigma(D)} \right)} \quad (B11)$$

and the electric field in region 2 can be expressed as

$$E_2(z) = \frac{\sigma_o}{\sigma(z)} \frac{V_o}{h \left(1 - \frac{\sigma_o}{\sigma(D)} \right)} \quad (B12)$$

Taking into account that $\sigma_o/\sigma(D) \ll 1$ the electric field at $z = 0$ can be found as $E_2 = E_1 \simeq V_o/h = 50 \text{ V m}^{-1}$ which is in good agreement with results of numerical calculations (Figure 30a).

The solution corresponding to $h_i \rightarrow 0$ closely resembles the "stationary" fair weather distribution of the electric field above the ground of the earth. Note that the numerical and analytical solutions are in good agreement at the final stage of establishment of this solution as can be seen in Figure 30a at $t \sim 100 \text{ s}$.

It follows from simple manipulations that the surface charges induced at the top $\rho_{s2} = -\varepsilon_o E_2(D, t)$ and at the bottom $\rho_{s1} = \varepsilon_o E_1(t)$ conducting surfaces, and the space charge induced in the region 2 $\rho_{\text{ind}} = \varepsilon_o \partial E_2 / \partial z$ at any moment of time satisfy the following condition:

$$\rho_{s1} + \rho_{s2} + \int_{h_i}^D \rho_{\text{ind}} dz = 0 \quad (B13)$$

showing that the total charge in the system is conserved.

Finally, to avoid any confusion, we note that in the real situation the potential difference V_o between the ground and the ionosphere is a slowly variable function of time [e.g., *Uman*, 1987] and the introduction of step like potential difference is considered in this appendix only for the purpose of providing physical insight into the problem (i.e., to give the simple one dimensional analytical illustration of the slowing down effect). Accordingly, it is clear that the solutions do not represent the actual dynamics of the establishment of the fair weather fields.

The amplitudes of fair weather electric fields are negligible in comparison with post discharge electric fields generated by thundercloud charges, so that the Earth's surface and the ionosphere with good accuracy may be considered to have the same potential (e.g., zero potential as assumed in our model). All physical effects described in this appendix pertain for two-dimensional case as was demonstrated by our numerical results (the analytical solution in the two-dimensional case is not known).

Acknowledgments.

This work was sponsored by NASA grants NAGW-2871-2 and NAGW-4738 to Stanford University. We greatly appreciate discussions with colleagues in the STAR Laboratory. Y. Taranenkov was supported by a LANL post-doctoral fellowship.

The Editor thanks D. D. Sentman and S. B. Mende for their assistance in evaluating this paper.

References

- Armstrong, R. A., J. Shorter, W. A. Lyons, L. Jeong, and W. A. M. Blumberg, Evidence of ionization in sprites N_2^+ 427.8 nm first negative emission measured in SPRITES'95 campaign, *Eos Trans. AGU*, 76(46), Fall Meet. Suppl., F114, 1995.
- Armstrong, W. C., Recent advances from studies of the Trimpf effect, *Antarc. J.*, 18, 281, 1983.
- Baginski, M. E., and A. S. Hodel, A case study comparing the lossy wave equation to the continuity equation in modeling late-time fields associated with lightning, *Appl. Comput. Electromagn. Soc. J.*, 9, 98, 1994.
- Baginski, M. E., L. C. Hale, and J. J. Olivero, Lightning-related fields in the ionosphere, *Geophys. Res. Lett.*, 15, 764, 1988.
- Bell, T. F., V. P. Pasko, and U. S. Inan, Runaway electrons as a source of Red Sprites in the mesosphere, *Geophys. Res. Lett.*, 22, 2127, 1995.
- Boccippio, D. J., E. R. Williams, S. J. Heckman, W. A. Lyons, I. T. Baker, and R. Boldi, Sprites, ELF transients, and positive ground strokes, *Science*, 269, 1088, 1995.
- Boeck, W. L., O. H. Vaughan Jr., R. Blakeslee, B. Vonnegut, and M. Brook, Lightning induced brightening in the airglow layer, *Geophys. Res. Lett.*, 19, 99, 1992.
- Boeck, W. L., O. H. Vaughan, R. J. Blakeslee, B. Vonnegut, M. Brook, and J. McKune, Observations of lightning in the stratosphere, *J. Geophys. Res.*, 100, 1465, 1995.
- Buneman, O., A compact non-iterative Poisson-solver, *SUIPR Rep.* 294, Stanford Univ., Stanford, Calif., 1969.
- Chamberlain, J. W., *Theory of Planetary Atmospheres*, Academic, San Diego, Calif., 1978.
- Davies, D. K., Measurements of swarm parameters in dry air, in *Theoretical Notes, Note 346*, Westinghouse R&D Center, Pittsburgh, Pa., May 1983.
- Dejnakarintra, M., and C. G. Park, Lightning-induced electric fields in the ionosphere, *J. Geophys. Res.*, 79, 1903, 1974.
- Dowden, R. L., C. D. C. Adams, J. B. Brundell, and P. E. Dowden, Rapid onset, rapid decay (RORD), phase and amplitude perturbations of VLF subionospheric transmissions, *J. Atmos. Terr. Phys.*, 56, 1513, 1994.
- Fishman, G. J., et al., Discovery of intense gamma-ray flashes of atmospheric origin, *Science*, 264, 1313, 1994.
- Fovell, R., D. Durran, and J. R. Holton, Numerical simulation of convectively generated stratospheric gravity waves, *J. Atmos. Sci.*, 49, 1427, 1992.
- Franz, R. C., R. J. Nemzek, and J. R. Winckler, Television image of a large upward electric discharge above a thunderstorm system, *Science*, 249, 48, 1990.
- Fukunishi, H., Y. Takahashi, M. Kubota, K. Sakanoe, U. S. Inan, and W. A. Lyons, Lightning-induced transient luminous events in the lower ionosphere, *Geophys. Res. Lett.*, 23, 2157, 1996.
- Glukhov, V. S., and U. S. Inan, Particle simulation of the time-dependent interaction with the ionosphere of rapidly varying lightning EMP, *Geophys. Res. Lett.*, 23, 2193, 1996.
- Green, B. D., M. E. Fraser, W. T. Rawlins, L. Jeong, W. A. M. Blumberg, S. B. Mende, C. R. Swenson, D. L. Hampton, E. M. Wescott, and D. D. Sentman, Molecular excitation in Sprites, *Geophys. Res. Lett.*, 23, 2161, 1996.
- Greifinger, C., and P. Greifinger, Transient ULF electric and magnetic fields following a lightning discharge, *J. Geophys. Res.*, 81, 2237, 1976.
- Gurevich, A. V., *Nonlinear Phenomena in the Ionosphere*, Springer-Verlag, New York, 1978.
- Gurevich, A. V., G. M. Milikh, and S. I. Shlyuger, Changing ionization of the lower ionosphere due to high-power radio waves, *Radiophys. Quantum Electron.*, 20, 1230, 1978.
- Hale, L. C., Coupling of ELF/ULF energy from lightning and MeV particles to the middle atmosphere, ionosphere, and global circuit, *J. Geophys. Res.*, 99, 21089, 1994.
- Hale, L. C., and M. E. Baginski, Current to the ionosphere following a lightning stroke, *Nature*, 329, 814, 1987.
- Hampton, D. L., M. J. Heavner, E. M. Wescott, and D. D. Sentman, Optical spectral characteristics of sprites, *Geophys. Res. Lett.*, 23(1), 89, 1996.
- Hegerberg, R., and I. D. Reid, Electron drift velocities in air, *Aust. J. Phys.*, 33, 227, 1980.
- Holden, D. N., C. P. Munson, and J. C. Devenport, Satellite observations of transionospheric pulse pairs, *Geophys. Res. Lett.*, 22, 889, 1995.
- Holzer, R. E., and D. S. Saxon, Distribution of electrical conduction currents in the vicinity of thunderstorms, *J. Geophys. Res.*, 57, 207, 1952.
- Holzworth, R. H., M. C. Kelley, C. L. Siefring, L. C. Hale, and J. T. Mitchell, Electrical measurements in the atmosphere and the ionosphere over an active thunderstorm, 2, Direct current electric fields and conductivity, *J. Geophys. Res.*, 90, 9824, 1985.
- Idone, V. P., A. B. Saljoughy, R. W. Henderson, P. K. Moore, and R. B. Pyle, A reexamination of the peak current calibration of the National Lightning Detection Network, *Geophys. Res. Lett.*, 98, 18323, 1993.
- Illingworth, A. J., Electric field recovery after lightning as the response of the conducting atmosphere to a field change, *Q. J. R. Meteorol. Soc.*, 98, 604, 1972.
- Inan, U. S., D. C. Shafer, W. Y. Yip, and R. E. Orville, Subionospheric VLF signatures of nighttime D-region perturbations in the vicinity of lightning discharges, *J. Geophys. Res.*, 93, 11455, 1988.
- Inan, U. S., T. F. Bell, and J. V. Rodriguez, Heating and ionization of the lower ionosphere by lightning, *Geophys. Res. Lett.*, 18, 705, 1991.
- Inan, U. S., J. V. Rodriguez, and V. P. Idone, VLF signatures of lightning-induced heating and ionization of the nighttime D-region, *Geophys. Res. Lett.*, 20, 2355, 1993.
- Inan, U. S., T. F. Bell, V. P. Pasko, D. D. Sentman, E. M. Wescott, and W. A. Lyons, VLF signatures of ionospheric disturbances associated with sprites, *Geophys. Res. Lett.*, 22, 3461, 1995.
- Inan, U. S., A. Slingeland, V. P. Pasko, and J. Rodriguez, VLF signatures of mesospheric/ lower ionospheric response to lightning discharges, *J. Geophys. Res.*, 101, 5219, 1996a.
- Inan, U. S., W. A. Sampson, and Y. N. Taranenko, Space-time structure of lower ionospheric optical flashes and ionization changes produced by lightning EMP, *Geophys. Res. Lett.*, 23, 133, 1996b.
- Inan, U. S., S. C. Reising, G. J. Fishman, and J. M. Horack, On the association of terrestrial gamma-ray bursts with lightning discharges and sprites, *Geophys. Res. Lett.*, 23, 1017, 1996c.
- Inan, U. S., V. P. Pasko, and T. F. Bell, 'Early/Fast VLF events as evidence of sustained heating of the ionosphere above thunderclouds, *Geophys. Res. Lett.*, 23, 1067, 1996d.
- Lehtinen, N. G., M. Walt, U. S. Inan, T. F. Bell, and V. P. Pasko, γ -ray emission produced by a relativistic beam of runaway electrons accelerated by quasi-electrostatic thundercloud fields, *Geophys. Res. Lett.*, 23, 2645, 1996.
- Lyons, W. A., Characteristics of luminous structures in the stratosphere above thunderstorms as imaged by low-light video, *Geophys. Res. Lett.*, 21, 875, 1994.
- Lyons, W. A., Low-light video observations of frequent luminous structures in the stratosphere above thunderstorms, *Mon. Weather Rev.*, 122, 1940, 1994.
- Lyons, W. A., Sprite observations above the U.S. high plains

- in relation to their parent thunderstorm systems, *J. Geophys. Res.*, in press, 1996.
- Malan, D. J., *Physics of Lightning*, The English Universities Press, London, 1963.
- Marshall, T. C., and W. D. Rust, Two types of vertical electrical structures in stratiform precipitation regions of mesoscale convective systems, *Bull. Am. Meteorol. Soc.*, **74**, 2159, 1993.
- Marshall, T. C., M. Stolzenburg, and W. D. Rust, Electric field measurements above mesoscale convective systems, *J. Geophys. Res.*, **101**, 6979, 1996.
- Mende, S. B., R. L. Rairden, G. R. Swenson, and W. A. Lyons, Sprite spectra: N₂ 1 PG band identification, *Geophys. Res. Lett.*, **22**, 2633, 1995.
- Meier, R. R., D. J. Strickland, J. H. Hecht, and A. B. Christensen, Deducing composition and incident electron spectra from ground-based auroral optical measurements: A study of auroral red line processes, *J. Geophys. Res.*, **94**, 13541, 1989.
- Milikh, G. M., K. Papadopoulos, and C. L. Chang, On the physics of high altitude lightning, *Geophys. Res. Lett.*, **22**, 85, 1995.
- Ogawa, T., Fair-weather electricity, *J. Geophys. Res.*, **90**, 5951, 1985.
- Orville, R. E., Calibration of a magnetic direction finding network using measured triggered lightning return stroke peak currents, *J. Geophys. Res.*, **96**, 17135, 1991.
- Papadopoulos, K., G. Milikh, A. Gurevich, A. Drobot, and R. Shanny, Ionization rates for atmospheric and ionospheric breakdown, *J. Geophys. Res.*, **98**, 17593, 1993.
- Pasko, V. P., and U. S. Inan, Recovery signatures of lightning-associated VLF perturbations as a measure of the lower ionosphere, *J. Geophys. Res.*, **99**, 17523, 1994.
- Pasko, V. P., U. S. Inan, Y. N. Taranenko, and T. F. Bell, Heating, ionization and upward discharges in the mesosphere due to intense quasi-electrostatic thundercloud fields, *Geophys. Res. Lett.*, **22**, 365, 1995.
- Pasko, V. P., U. S. Inan, and T. F. Bell, Sprites as luminous columns of ionization produced by quasi-electrostatic thundercloud fields, *Geophys. Res. Lett.*, **23**, 649, 1996a.
- Pasko, V. P., U. S. Inan, and T. F. Bell, Blue jets produced by quasi-electrostatic pre-discharge thundercloud fields, *Geophys. Res. Lett.*, **23**, 301, 1996b.
- Potter, D., *Computational Physics*, John Wiley, New York, 1973.
- Picard, R. H., J. R. Winick, R. D. Sharma, A. S. Zachor, P. J. Espy, and C. R. Harris, Interpretation of infrared measurements of the high-latitude thermosphere from a rocket-borne interferometer, *Adv. Space Res.*, **7**(10), 23, 1987.
- Rairden, R. L., and S. B. Mende, Time resolved sprite imagery, *Geophys. Res. Lett.*, **22**, 3465, 1995.
- Reid, G. C., The middle atmosphere, NASA Conf. Publ., NASA CP-2090, 27-42, 1979.
- Roussel-Dupre, R. A., and A. V. Gurevich, On runaway breakdown and upward propagating discharges, *J. Geophys. Res.*, **101**, 2297, 1996.
- Rowland, H. L., R. F. Fernsler, J. D. Iluba, and P. A. Bernhardt, Lightning driven EMP in the upper atmosphere, *Geophys. Res. Lett.*, **22**, 361, 1995.
- Rowland, H. L., R. F. Fernsler, and P. A. Bernhardt, Breakdown of the neutral atmosphere in the D-region due to lightning driven electromagnetic pulses, *J. Geophys. Res.*, **101**, 7935, 1996.
- Rust, W. D., T. C. Marshall, M. Stolzenburg, M. G. Bote-man, T. R. Shepherd, and B. F. Smull, Observations of electrical structure of midlatitude mesoscale convective systems: Review and update, in *Proceedings of 10th International Conference on Atmospheric Electricity*, p. 108, Osaka, 1996.
- Sentman, D. D., and E. M. Wescott, Observations of upper atmospheric optical flashes recorded from an aircraft, *Geophys. Res. Lett.*, **20**, 2857, 1993.
- Sentman, D. D., and E. M. Wescott, Red sprites and blue jets, Geophys. Instit. Video Prod., Univ. of Alaska, Fairbanks, July 9, 1994.
- Sentman, D. D., and E. M. Wescott, Red sprites and blue jets: Thunderstorm-excited optical emissions in the stratosphere, mesosphere, and ionosphere, *Phys. Plasmas*, **2**, 2514, 1995.
- Sentman, D. D., E. M. Wescott, D. L. Osborne, D. L. Hampton, and M. J. Heavner, Preliminary results from the Sprites94 campaign: Red Sprites, *Geophys. Res. Lett.*, **22**, 1205, 1995.
- Sipler, D. P., and M. A. Biondi, Measurements of O(¹D) quenching rates in the F region, *J. Geophys. Res.*, **77**, 6202, 1972.
- Swarztrauber, P., and R. Sweet, Efficient FORTRAN subprograms for the solution of elliptic partial differential equations, *NCAR Tech. Note*, NCAR/TN-109+IA, July 1975.
- Taranenko, Y. N., Interaction with the lower ionosphere of electromagnetic pulses from lightning: Heating, attachment, ionization, and optical emissions, Ph.D. dissertation, Stanford Univ., Calif., Sept. 1993.
- Taranenko, Y. N., and R. A. Roussel-Dupre, High altitude discharges and gamma-ray flashes: a manifestation of runaway air breakdown, *Geophys. Res. Lett.*, **23**, 571, 1996.
- Taranenko, Y. N., U. S. Inan, and T. F. Bell, Interaction with the lower ionosphere of electromagnetic pulses from lightning: Heating, attachment, and ionization, *Geophys. Res. Lett.*, **20**, 1539, 1993a.
- Taranenko, Y. N., U. S. Inan, and T. F. Bell, The interaction with the lower ionosphere of electromagnetic pulses from lightning: Excitation of optical emissions, *Geophys. Res. Lett.*, **20**, 2675, 1993b.
- Taylor, L. L., Mesospheric heating due to intense tropospheric convection, *NASA Contract. Rep.*, 3132, 1979.
- Tzur, I., and R. G. Roble, The interaction of a polar thunderstorm with its global electrical environment, *J. Geophys. Res.*, **90**, 5989, 1985.
- Uman, M. A., The Earth and its atmosphere as a leaky spherical capacitor, *Am. J. Phys.*, **42**, 1033, 1974.
- Uman, M. A., *The Lightning Discharge*, Academic, San Diego, Calif., 1987.
- Valence-Jones, A., *Aurora*, D. Reidel, Norwell, Mass., 1974.
- Vaughan, O. H., Jr., R. J. Blakeslee, W. L. Boeck, B. Vonnegut, M. Brook, and J. McKune Jr., A cloud-to-space lightning as recorded by the space shuttle payload-bay TV cameras, *Mon. Weather Rev.*, **120**, 1459, 1992.
- Walterscheid, R. L., and G. Schubert, Nonlinear evolution of an upward propagating gravity wave: overturning, convection, transience and turbulence, *J. Atmos. Sci.*, **47**, 101, 1990.
- Wen, C., and J. M. Wetzler, Electron avalanches influenced by detachment and conversion processes, *IEEE Trans. Electr. Insul.*, **23**, 999, 1988.
- Wescott, E. M., D. Sentman, D. Osborne, D. Hampton, and M. Heavner, Preliminary results from the Sprites94 aircraft campaign, 2, Blue jets, *Geophys. Res. Lett.*, **22**, 1209, 1995a.
- Wescott, E. M., D. D. Sentman, M. J. Heavner, and D. L. Hampton, Blue starters, discharges above an intense thunderstorm over Arkansas, July 1, 1994, *Eos Trans. AGU*, **76**, (46), Fall Meet. Suppl., F104, 1995b.

- Wescott, E. M., D. D. Sentman, M. J. Heavner, D. L. Hampton, D. L. Osborne, and O. H. Vaughan Jr., Blue Starters: Brief upward discharges from intense arkansas thunderstorm, *Geophys. Res. Lett.*, **23**, 2153, 1996.
- Wilson, C. T. R., The electric field of a thundercloud and some of its effects, *Proc. Phys. Soc. London*, **37**, 32D, 1925.
- Wilson, C. T. R., A theory of thundercloud electricity, *Proc. R. Soc. London Ser. A*, **236**, 297, 1956.
- Winckler, J. R., Further observations of cloud-ionosphere electrical discharges above thunderstorms, *J. Geophys. Res.*, **100**, 14335, 1995.
- Winckler, J. R., W. A. Lyons, T. Nelson, and R. J. Nemzek, New high-resolution ground-based studies of cloud- ionosphere discharges over thunderstorms (CI or Sprites), *J. Geophys. Res.*, **101**, 6997, 1996.
- T. F. Bell, U. S. Inan, and V. P. Pasko, STAR Laboratory, Stanford University, Stanford, CA 94305.
- Y. N. Taranenko, XCM, Computational Science Methods, MS-F645, Los Alamos National Laboratory, Los Alamos, NM 87545.

(Received April 9, 1996; revised November 8, 1996; accepted November 8, 1996.)